SAND79-8062
Unlimited Release

Calculation of Skin-Friction Coefficients for Low-Reynolds-Number Turbulent Boundary Layer Flows

MASTER

P. K. Barr

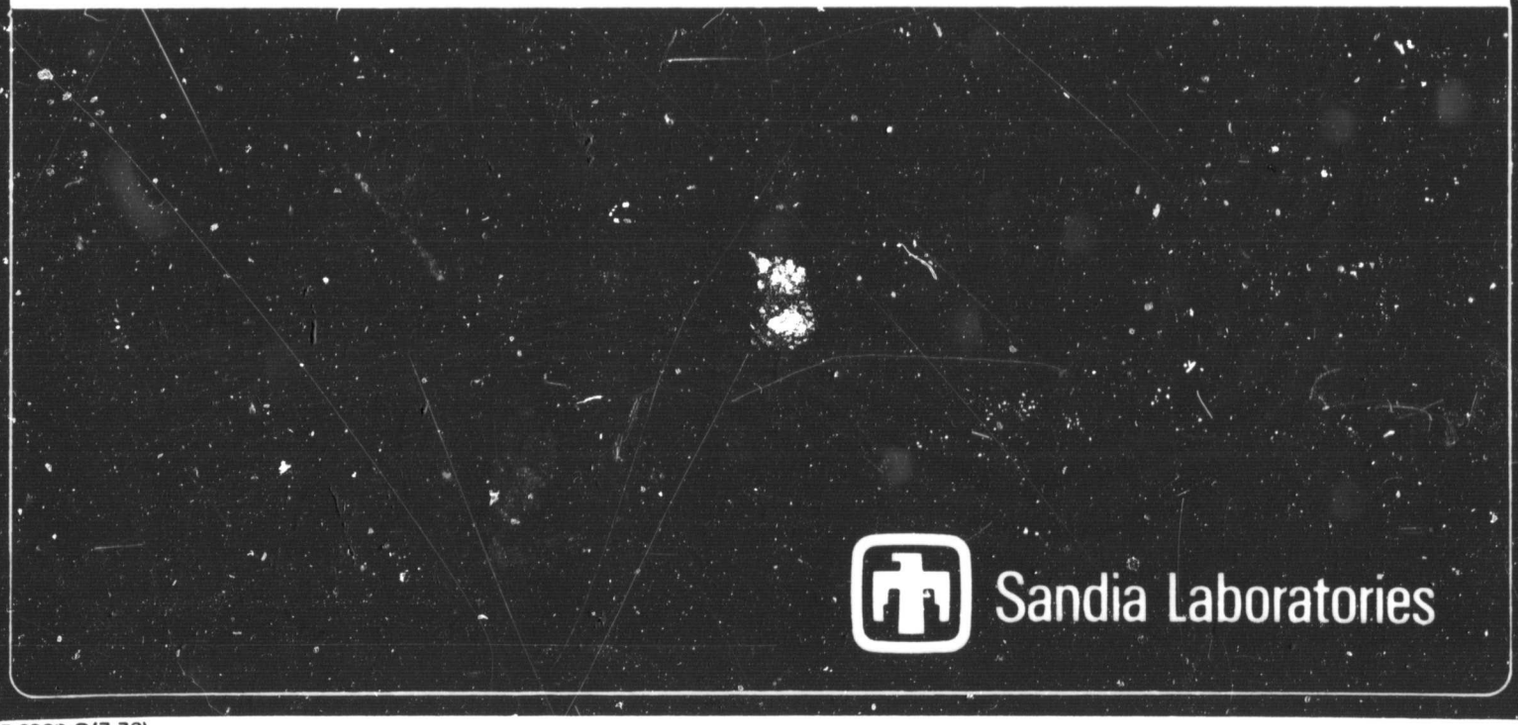

SF 2900 Q(7-73)

Page intentionally left blank

SAND79-8062
Unlimited Release
Printed January 1980

CALCULATION OF SKIN-FRICTION COEFFICIENTS FOR LOW-REYNOLDS-NUMBER TURBULENT BOUNDARY LAYER FLOWS

Pamela K. Barr
Gas Dynamics Division 8354

ABSTRACT

This paper presents an analysis of the reliability of various generally accepted empirical expressions for the prediction of the skin-friction coefficient C_f of turbulent boundary layers at low Reynolds numbers in zero-pressure-gradient flows on a smooth flat plate. The skin-friction coefficients predicted from these expressions were compared to the skin-friction coefficients of experimental profiles that were determined from a graphical method formulated from the law of the wall. These expressions are found to predict values that are consistently different than those obtained from the graphical method over the range $600 < Re_\theta < 2000$. A curve-fitted empirical relationship was developed from the present data and yields a better estimated value of C_f in this range.

The data, covering the range $200 < Re_\theta < 7000$, provide insight into the nature of transitional flows. They show that fully developed turbulent boundary layers occur at Reynolds numbers Re_θ down to 425. Below this level there appears to be a well-ordered evolutionary process from the laminar to the turbulent profiles. These profiles clearly display the development of the turbulent core region and the shrinking of the laminar sublayer with increasing values of Re_θ.

CONTENTS

ILLUSTRATIONS

ILLUSTRATIONS (continued)

NOMENCLATURE

B	additive constant appearing in the law of the wall
C	pressure coefficient
C_f	skin-friction coefficient = $\tau_w/(\frac{1}{2}\rho U_\infty^2)$
c_p	specific heat
D	Pitot probe diameter = 0.0425 cm
E_s	error term, defined by Eq. (12)
H	shape factor = δ^*/θ
H_o	chamber pressure
k_s	average height of sand grain roughness elements
$k+$	roughness factor = $k_s V+/\nu$
M	Mach number
P_o	stagnation pressure
Re_D	Reynolds number = Du/ν
Re_x	Reynolds number = xU_∞/ν
Re_y	Reynolds number = yU_∞/ν
Re_θ	Reynolds number = $\theta U_\infty/\nu$
T	temperature
T_o	stagnation temperature
u	local velocity in the streamwise direction
u_w	slip velocity
U_∞	free-stream velocity

V^*	friction speed = $\sqrt{\tau_w/\rho} = U_\infty\sqrt{C_f/2}$
x	streamwise coordinate
y	direction normal to surface
γ	ratio of specific heats = c_p/c_v
δ	boundary layer thickness (99% free-stream)
δ^*	displacement thickness = $\int_0^\delta (U_\infty - u)/U_\infty \, dy$
ΔP	pressure differential
Θ	momentum thickness = $\int_0^\delta (u/U_\infty)(U_\infty - u)/U_\infty \, dy$
κ	von Kármán constant appearing in the law of the wall
λ	molecular mean free path
μ	dynamic viscosity
ν	kinematic viscosity
ρ	fluid density
τ_w	wall shear stress

ACKNOWLEDGMENTS

This work was also submitted in partial satisfaction of the requirements for the Master of Science degree at the University of California at Davis. It was supported by the Office of Planetary Geology, National Aeronautics and Space Administration, through Interchange Agreement NCA2-OR 180-704 to the University of California at Davis, and NASA-Ames Research Center, Moffett Field. Appreciation is extended to Mr. Chi T. Tran for his work on the velocity reduction program and special thanks to Dr. Bruce R. White for his advice and patience in this research effort.

CALCULATION OF SKIN-FRICTION COEFFICIENTS FOR LOW-REYNOLDS-NUMBER TURBULENT BOUNDARY LAYER FLOWS

Introduction

This paper presents an analysis of the reliability of various methods of predicting the skin-friction coefficient for turbulent boundary layers at low Reynolds numbers, $600 < Re_\theta < 2000$. These methods include the expressions developed by White (1974), Ludwieg & Tillmann (1950), and the 1/7th-power-law formulation (Schlichting, 1968). These methods are shown to be inadequate in this limited range and have led to the development of a new expression based on experimental data covering this range.

This research stems from the investigation of eolian processes on the surface of Mars. The atmospheric boundary layers are turbulent in nature and occur in the lower Reynolds numbers because of the low densities. The minimum value of surface shear stress necessary to move particles on Mars may be estimated from experimentally determined skin-friction coefficients C_f presented in this paper. This work may also prove useful for making estimates of erosion rates occuring on Mars.

Many of the wind tunnel experiments performed resulted in profiles that were not fully turbulent. These flows had values of Re_θ down to 200. They provide a unique opportunity to observe the general nature of transition from a laminar profile to a fully turbulent one.

Background

That particle movement of soil by atmospheric winds is important to various geological processes is easily observed. The soil movement is seen in dust storms, and its effects are seen in the shifting sand dunes along with other indications of erosion and deposition in the arid regions on Earth. The transport of particles by the wind is manifested in any of three processes. The sliding of particles along the surface is known as creep or surface traction. Other particles are suspended within the wind and only touch ground after long periods of time aloft. Most commonly on Earth, particles are moved by a bouncing or leaping motion called saltation. The impact of the saltating strains can initiate the other two processes. In order for particles to be picked up and set in motion, a strong wind is required.

A major contributor in the field of eolian processes is R. A. Bagnold, who lead the way in 1941 with a book devoted to the subject. His work, based on wind-tunnel studies and field observations, describes the basics of sand movement by winds for environments found on Earth.

Eolian processes are not limited to Earth. For centuries, many astronomers have observed dust storms on Mars. Their existence has been confirmed by the images sent back by the Viking and Mariner spacecraft. These images clearly show that the wind is the dominant agent of erosion (depletion and abrasion) on Mars. Although Mars, like the Earth, contains an atmosphere, the results found on Earth cannot be extended to applications to Mars without considering the physical differences.

The major differences between the atmospheres of Mars and Earth which are of concern in the study of the physics of wind action are drastic. The Martian atmospheric pressure ranges from 0.3 to 1.0% of that on Earth. The composition of the atmosphere of Mars is 96% carbon dioxide, with nitrogen and argon accounting for only 2.2 and 1.5%, respectively (Owen & Bierman, 1976). Air is composed of 76% nitrogen and 23% oxygen by weight. Although the temperatures are somewhat similar, ranging from approximately 150 to 300 K on Mars (Hess et al., 1976), the gas densities are markedly different. These very low densities on Mars cause the atmospheric boundary layers to occur in the low-Reynolds-number range. They are turbulent because of the planet's rugged surface topography.

The reduced pressures result in larger wind speeds needed to set particles in motion. The minimum wind speed necessary to create particle motion is dependant on the particle size and weight and the surface shear stress, which depends on the fluid density and viscosity. Using the friction speed V*, defined as

$$V^* = \sqrt{\tau_w/\rho}, \tag{1}$$

where τ_w is the surface shear stress and ρ is the fluid density, this minimum wind speed can be represented by a threshold friction speed. This friction speed is dependant upon the characteristics of the wind boundary layer. In order to estimate the importance of eolian activity on Mars, it is essential to accurately predict the friction speeds found in the Martian environment.

Although some studies of the turbulent boundary layer on a flat plate at low Reynolds numbers exist, none deal with the determination of the skin-friction coefficient in this narrow range of boundary layer studies. Little experimental data is found in the literature for this range.

For the wall shearing stress in turbulent boundary layers, some researchers report analytical approximations which are supposedly valid for the lower Reynolds numbers (see Appendix A). These expresssions are developed, however, to cover a wide range of flows. Since they are not exclusively devoted to the range applicable to Mars, usually few data in the lower range were used to develop the expressions. Thus, the reliability of these methods to predict friction velocities accurately in this range is questionable.

In order to check the reliability of some of these approximations, wind-tunnel experiments were conducted to correlate skin-friction coefficients with the boundary layer profiles at the lower Reynolds numbers.

Data Aquisition and Computer Analysis

I. Obtaining the Velocity Profiles

The experimental data were obtained through an interchange agreement between the University of California and NASA's Ames Research Center in Moffett Field, California. The profiles were taken in conjunction with other experiments, and as a result, there was no control over experimental conditions or procedures. The tests were conducted at low pressures, thus resulting in low densities and large kinematic viscosities. High free-stream velocities were used and the resulting profiles had large boundary layer thicknesses. In order to obtain the same Reynolds number flows at atmospheric pressure, the flow would have to move much slower and the boundary layer heights would be greatly reduced, resulting in a considerable loss of accuracy in the data. A description of the experimental facility is presented in Appendix B, and a more detailed one can be found in the paper by Greeley et al. (1977).

The bounday layer profiles were recorded in pairs. The first profile was obtained with the Pitot probe starting from the center of the tunnel and traveling down to the floor. It took approximately one minute for the probe to travel through the boundary layer, a height of roughly 20 cm. The second profile was measured with the probe traveling from the tunnel floor back to free stream. Although a constant ambient pressure and free-stream velocity was desired, occasionally the background conditions drifted during the recording of a profile. Because of the possibility of the drifting, each profile traverse was analyzed separately. If either the free-stream velocity or the ambient pressure varied from the mean value for that run by more than 7.5%, that run was rejected for analysis.

It was desired to find the mean turbulent velocity profile. An example of the pressure differential profile is shown in Figure 1. As can be seen from the figure, this profile contains many fluctuations around a mean value. The time-averaged profiles were drawn on the strip chart recordings by hand so that the turbulent fluctuations were smoothed out. This effectively set the mean profile. The smoothed profile is also shown in Figure 1. Data points were then recorded from the smoothed curve at evenly spaced intervals and the data keypunched for later use in the computer analysis.

Studies of the strip chart recordings of the boundary layer data show that these profiles contain lower-frequency fluctuations characteristic of larger sized turbulent eddies. Although the smaller-scale variations cause no problems, the larger fluctuations can cause the interpretation of the mean velocity profile to be somewhat in error. The only runs analyzed were those with clear mean velocity profiles. These runs were also required to have background pressures that did not vary throughout the run by more than 15%, did not appear to be troubled by slow responses in the measurement system, and had no noticeable large-scale fluctuations.

Each profile data set consists of at least 20 readings, each containing a probe height and the corresponding Pitot tube pressure differential reading. The ambient chamber pressure and stagnation temperature were independently recorded on separate equipment. The velocity for each height was found in the following manner (a more thorough description is presented in Appendix C):

(i) The theoretical velocity is calculated, including Mach number effects and ignoring corrections for viscous effects on the measurement system.

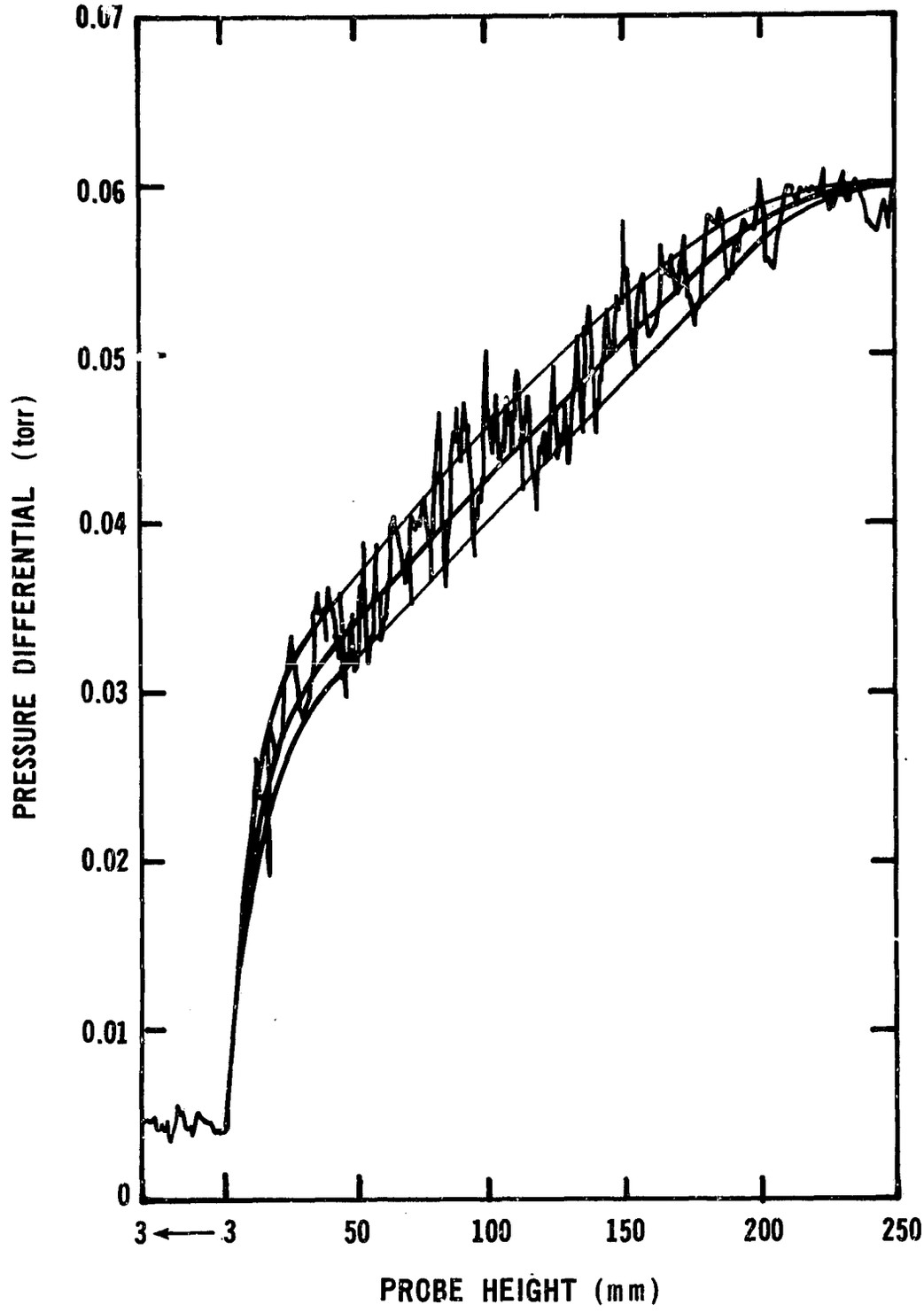

Figure 1

Example of instantaneous pressure differential profile showing mean profile (center line) and the error bounds for the mean profile (outer lines). Note the minimum probe height is 3 mm for this run.

(ii) A pressure coefficient C, which takes into account viscous effects on the probe, is calculated based on the Reynolds number, $Re_D = Du/\nu$, where D is the Pitot tube diameter and u is the local velocity.

(iii) Using this coefficient the actual velocity is found from the correction to the theoretical velocity.

(iv) From this velocity, the temperature, viscosity, density, and Mach number are again computed.

Each set of profile data, consisting of a height and the corresponding velocity, is normalized based on a height of the 99% boundary layer thickness and the free-stream velocity.

II. Determination of δ^* and Θ

Many of the empirical methods of estimating the skin-friction factors are based on the displacement thickness δ^* and momentum-deficit thickness Θ, (i.e., those listed Appendix A). These thicknesses are found from the integration of the velocity profile, as defined in the nomenclature. The use of the integral parameters δ^* and Θ is preferred because of the accuracy by which they may be determined relative to the initial profile.

A common method of integration of a function defined by a set of unevenly spaced points, such as a set of data points, would be the integration of a smooth, continuous curve which fits the points. In order to evaluate these integral parameters, the velocity profiles were fitted with a smooth continuous curve. The curve fit method chosen is a least-squares approximation by cubic splines with a given number of knots, a knot being the endpoint of a section fit by a cubic.

The most common form of the cubic spline is one which fits a cubic to each adjacent pair of data points. This fit, which treats each data point as a knot, matches first and second derivatives at the knots and satisfies given end conditions. Thus the number of data points, and also the number of knots, equals the number of cubics plus one. This type of fit is forced through each data point. It is primarily used to interpolate between tabulated points.

The actual curve fit method chosen is closely related to the common cubic spline. In order to smooth out variations in the data caused by any number of factors, including the accuracy involved in reading strip-chart recordings, the number of knots can be greatly reduced and their location varied until a suitable fit is found. The optimum location of the knots would be that which minimizes the least-squares error of the curve fit. From trial and error, it was found that a four-piece fit was sufficient to provide a nice fit of the data as determined by eye. The cubic spline routine selected, ICSVKU, is a part of the IMSL scientific library.†

A conventional ploynomial fit using the least-squares error criteria was tried, without success, because of the difficulties involved in providing a smooth fit to a curve which tends to have an "elbow" shape. This bend is caused by the joining of the viscous sublayer and the turbulent core, a trait of turbulent boundary layers. In an attempt to fit the data, polynomials of order three and higher were tried. All, however, resulted in extreme inflections in the curve fit, as can be seen in Figure 2, a typical turbulent boundary layer profile fit with a fifth order polynomial.

---

†Available from IMSL
Sixth Floor, GNS Building
7500 Bellaire Boulevard
Houston, Texas 77036
(713/772-1927)

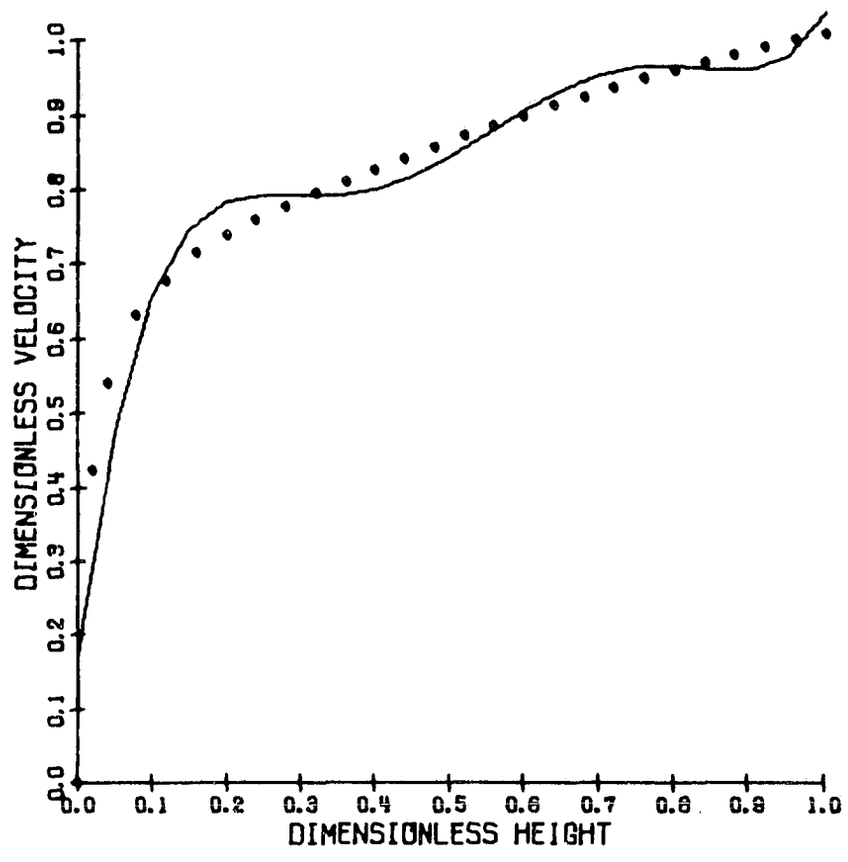

Figure 2

Typical turbulent velocity profile (data points) fitted with a fifth-order polynomial (solid line).

The dimensionless displacement thickness δ^*/δ, defined as

$$\delta^*/\delta = \int_0^1 (U_\infty - u)/U_\infty \, d(y/\delta)$$

$$= 1 - \int_0^1 u/U_\infty \, d(y/\delta), \qquad (2)$$

is found by integrating the curve fit with the aid of another IMSL routine entitled DCSQDU which integrates a cubic spline. The dimensionless momentum-deficit thickness Θ/δ may be simplified to

$$\Theta/\delta = \int_0^1 (u/U_\infty)(U_\infty - u)/U_\infty \, d(y/\delta)$$

$$= \int_0^1 (u/U_\infty) \, d(y/\delta) - \int_0^1 (u/U_\infty)^2 \, d(y/\delta) \, . \qquad (3)$$

It was found by integrating the square of the dimensionless velocity profile using a Newton-Cotes quadrature formula of the seventh order as explained in Appendix D. As a check, this method was also used to integrate the velocity profile, and the result agreed with the IMSL solution to eight-place accuracy in every profile analyzed.

Using the shape factor H and the Reynolds number based on momentun-deficit thickness Re_θ, skin-friction coefficients C_f were calculated from various approximate expressions by White, Ludwieg and Tillmann, and the 1/7th--power law approximation (see Appendix A). These equations should be valid in the low-Reynolds-number range for turbulent boundary layers on a smooth flat plate, at least to the lower limits of Re_θ as reported in the referenced papers.

III. Roughness Effects

Though insignificant in laminar flow, roughness effects strongly influence turbulent flow. In laminar flow the entire boundary layer is dominated by viscous effects. In turbulent flow, however, the viscous influence is limited to the viscous sublayer. Thus small roughness elements can drastically alter the velocity profile by breaking up the viscous layer.

As described in Schlichting (1968), three basic regimes of roughness influence exist. Defining a roughness factor k+ as $k_s V^*/\nu$, where k_s denotes the mean grain height, these three regions may be summarized as follows:

(i) Hydraulically smooth regime:

$0 \leq k+ \leq 5$.

All protrusions are contained within the viscous sublayer. The skin-friction coefficient is only a function of Reynolds number.

(ii) Transition regime:

$5 \leq k+ \leq 70$.

Protrusions would extend outside the viscous sublayer, causing it to break up before it fully developed. The skin-friction coefficient is dependent on both the Reynolds number and the size of the roughness element.

(iii) Completely rough regime:

$k+ > 70$.

The roughness elements cause the viscous sublayer to break up, and the flow near the wall is independent of viscosity. Here, C_f is only a function of the roughness size.

Thus, in order for the flow to be considered hydraulically smooth, it must satisfy the criterion $k+ \leq 5$.

The profiles were taken in the wind tunnel on a flat plate floor covered with sand with a mean diameter of 0.06 cm. It was necessary to confirm the smooth plate assumption because of the presence of these sand grains. The roughness factor k+ was evaluated for all runs using the friction speed found from the "exact" value of C_f (determined in the next section). The majority of the data are well within the smooth regime. Of more than 60 runs examined, only the four highest Reynolds number flows ($4500 \leq Re_\theta \leq 7000$) were out of the smooth floor regime, with the roughness factor reaching a maximum value of 7.7. However, the main focus here is $Re_\theta < 2000$, and these runs do not tend to differ from the conventional theory. These runs were included in the data set as establishing the reliability of the wind tunnel. Hence, an extension into the range $Re_\theta < 2000$ could be made with some confidence.

Theory

The evaluation of existing expressions for the skin-friction coefficient requires a reliable method of determining a reference value. This reference can then be used to develop a new expression if needed.

The skin-friction coefficient is defined as

$$C_f = 2\,\tau_w / (\rho\, U_\infty^2) \ ,$$

where

$$\tau_w = \mu \left.\frac{\partial u}{\partial y}\right|_w \ . \qquad (4)$$

As pointed out in Coles & Hirst (1968), one method of determining the friction coefficient is to estimate the slope of the velocity profile at the wall. This method requires a very accurate profile in the near-wall region. As can be seem from the form of the raw data shown in Figure 1 where the velocity is directly related to the pressure differential, an approach of this form for these data would not yield accurate enough results to use as a reference, although they do produce values which can be used to support other methods.

Ludwieg & Tillmann (1950) pointed out that all turbulent boundary layers with the presence of any pressure gradient near a smooth wall coincide with the universal line of u/V* versus log (yV*/ν). The form of this relation is commonly known as the law of the wall and can be written as

$$\frac{u}{U_\infty} = \frac{V^*}{U_\infty}\ \frac{2.30}{\kappa} \log_{10} (yV^*/\nu) + B \ , \qquad (5)$$

where $\kappa = 0.418$ and $B = 5.45$ (Patel, 1965). Using the fact that $u/V^* =$

$u/U_\infty \sqrt{2/C_f}$, Clauser (1954) developed a family of curves which use C_f as the parameter. For a single velocity profile, the experimental data can be plotted on this family of curves and a value of C_f selected which best fits the data. The simplicity of this approach is shown in the equation

$$\frac{u}{U_\infty} = \frac{\sqrt{C_f}}{2} \; 5.5 \log_{10} (Re_y \sqrt{C_f/2}) + 5.45 \quad . \qquad (6)$$

A plot of these curves, shown in Figure 3, can then be used as a method of determining the value of the skin-friction coefficient C_f for fully developed turbulent boundary layers, provided the flow behaves in accordance with the law of the wall. This method, known henceforth as the Clauser method, has the advantage of using more of the profile in the determination of C_f and using the turbulent core region, which represents roughly the lowest 20% of the boundary layer, rather than relying only on the scarce data within the viscous sublayer. Also, it is fairly easy to use, requiring only that the experimental data be plotted as u/U_∞ versus log $(y/U_\infty/\nu)$.

The Clauser method was used to determine the experimental values of C_f for the velocity profiles. The values of C_f determined by this technique are assumed to be the most accurate experimentally determined values, and are termed the "exact" values, although C_f is not directly measured.

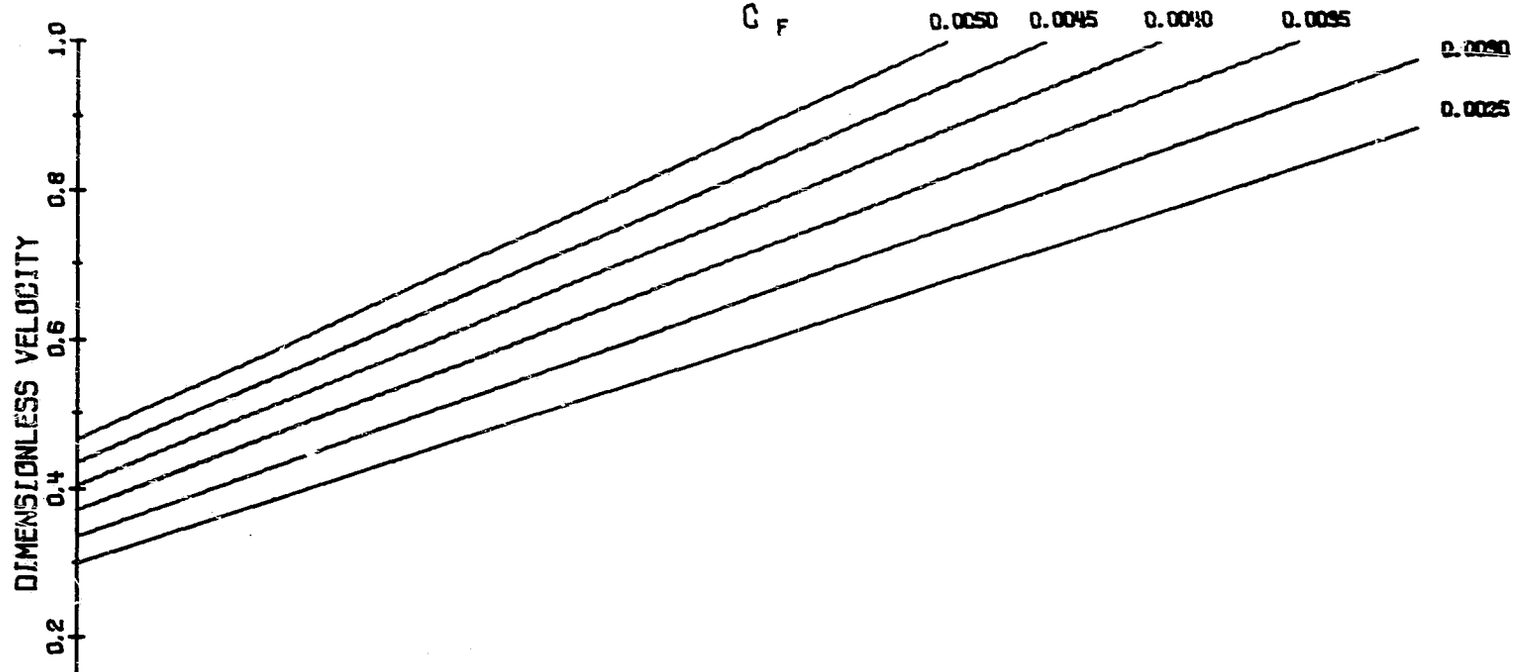

Figure 3

Lines of constant C_f from Eq. (6), the Clauser method.

Expected Accuracy of Profiles

The main advantage of the low-pressure chamber for wind-tunnel testing is the resulting increased boundary layer heights for comparable Reynolds numbers at atmospheric pressures. The gas density ρ is lower and the kinematic viscosity ν much higher at reduced pressures than at atmospheric pressures. Although the densities are extremely low, the viscous slip along the wall is negligible, as shown in Appendix E.

Assuming the 1/7th-power-law velocity distribution for turbulent flow, an expression for the boundary layer thickness can be obtained as (Schlichting, 1968)

$$\delta = 0.37 \times (xU_\infty/\nu)^{-1/5} \quad . \tag{7}$$

At atmospheric pressure, air at 25°C has a viscosity $\nu = 1.52$ m^2/s. However, when the pressure of air is reduced to 7.5% atmospheric, still at 25°C, the kinematic viscosity increases to 20,7000 m^2/s more than 10,000 times larger. It is obvious that for the same Reynolds number Re_x, the velocity of the reduced pressure flow cannot increase by this same factor. The relative distance x must also change to accommodate this increase in viscosity. However, the extra factor of x in Eq. (7) causes the boundary layer thickness to increase also. Typical boundary layer thicknesses are from 17 to 21 cm for velocity profiles measured at low pressures.

Previous data for Reynolds numbers based on momentum-deficit thickness Re_Θ less than 10,000 show that the boundary layer height is seldom greater than 5 cm; for $Re_\Theta < 1000$, δ is usually less than 1 cm. This can be seen in the data tabulated by Coles & Hirst (1968) from the Stanford Conference. Thus, the accuracy by which the velocity profile can be measured should be much greater because of the magnification of the fluid speeds and boundary

layer heights at the low pressures. Although other researchers have obtained limited data for Reynolds numbers less than 2000, it is expected that their results generally are not as accurate as those which are presented here.

As a result of the size and amount of fluctuation in the instantaneous velocity profile, it was feared that the initial hand-smoothing technique would introduce errors into the data reduction. As can be seen from Figure 1 it is rather difficult to place the mean velocity profile accurately. Sensitivity studies were conducted which showed that this was not a problem. Ten runs were chosen, representing a variety of Reynolds numbers in both air and CO_2, each of which was reduced using three different shapes of the smoothed curve. The three included an upper, middle, and lower estimate of the mean curve, as shown in Figure 1. The two extreme estimates of the mean profile are certainly in error and should provide reasonable estimates of error bound limits. Each of these three curves was assumed to have the same free-stream velocity and ambient pressure since these are most accurately known.

It was found that the shape factor never varied from the highest to the lowest value by more than 5% in each run, and typically was less than 3%. This implies that the values of H found from the mean profile can be believed to be accurate to within $\pm$1.5-2.5%. The Reynolds number Re_Θ has a maximum variation from the upper to the lower error bound limits of not more than 20%, typically 17-18%, hence the experimental values can be trusted to better than $\pm$10% since they should be better than the extreme error limit curves presented here. The higher variation in the Reynolds numbers relative to the shape factor H is caused by the different boundary layer thicknesses δ produced by each of these extreme cases. As can be seen from Figure 1, by assuming the same free-stream ΔP the lower estimate has a greater boundary layer thickness than the upper estimate. It was found that the variations in

the dimensionless displacement and momentum-deficit thicknesses were much less than the variation in boundary layer height. However, when evaluating the shape factor, the boundary layer thickness cancels out, thus reducing the variations the shape factor relative to the Reynolds number. The skin-friction coefficient found by the Clauser method was accurate to $\pm$5% of the value found by the "conventional" mean velocity profile. This is consistent with the scatter seen in the C_f data presented in the next section. It shows a variation of less than 5% at any Reynolds number.

Results and Discussion

Overall Description of the Profiles

The studies of smooth-flat-plate turbulent-boundary-layer profiles were grouped into four categories: (i) the higher Reynolds number region ($Re_\theta > 2000$), which is fairly well documented, (ii) the low-Reynolds-number range ($600 < Re_\theta < 2000$) containing fully developed turbulent profiles, (iii) those for very low Reynolds numbers ($425 < Re_\theta < 600$) which are fully developed but not characterized by the law of the wall, and (iv) the lowest Reynolds numbers ($200 < Re_\theta < 425$) which are not fully turbulent but show the development of the turbulent layer through the transition phase. Enough data were obtained to summarize basic characteristics of each group. Since the bulk of the data is in the second group, a more detailed treatment of it will follow.

(i) $Re_\theta > 2000$. Flows in this range blend with previous data when comparing basic parameters such as skin-friction coefficients and characteristic values of δ^*/δ and θ/δ for similar values of Reynolds numbers. All are well modeled by the law of the wall, displaying the logarithmic behavior of the turbulent core region.

The skin-friction coefficients are well predicted by already existing expressions such as those found in Appendix A. The importance of these runs is in confirming the credibility of the boundary layer flow in the wind tunnel.

(ii) $600 < Re_\theta < 2000$. A typical plot of u/U_∞ versus log (yU_∞/ν) for Re_θ = 775 is shown in Figure 4. Also shown are the lines of constant C_f. The profile, taken at 1.2% atmospheric pressure in air, shows a moderate wake region and viscous sublayer. This flow has a shape factor of 1.46 and a boundary layer height δ of 21.5 cm. It was taken at a free-stream velocity of 41.6 m/s and a kinematic viscosity of 12.5 cm^2/s. The Clauser method predicts a C_f of 0.00467, whereas the methods by White, Ludwieg & Tillmann, and the 1/7th-power law predict it to be 0.00421, 0.00424, and 0.00482, respectively. From Figure 6 it can be seen that the turbulent core region displays the law-of-the-wall behavior. Figure 5 shows the dimensionless velocity u/U_∞ versus dimensionless height y/δ. This plot shows a large buffer region, as described in Kline et al., (1967), which extends to y/δ = 0.1. Although the large size of this region is displayed in many profiles in this Reynolds number range, the customarily smaller buffer layer is observed in the other half of these flows.

Values of the skin-friction coefficient were also determined from the viscous sublayer in the velocity profile using

$$C_f = \frac{2\nu}{U_\infty} \frac{\partial u}{\partial y}\bigg|_w \quad . \tag{8}$$

Although this method is not as accurate as the Clauser method, the values of C_f calculated from the velocity slope at the wall do agree with those found by the graphical method. This supports the validity of the universal velocity profile in this range, implying that the constants used in the law-of-the-wall expression, Eq. (5), do not appear to deviate from the values κ = 0.418 and B = 5.45 for these low-Reynolds-number profiles. This contradicts the conclusion

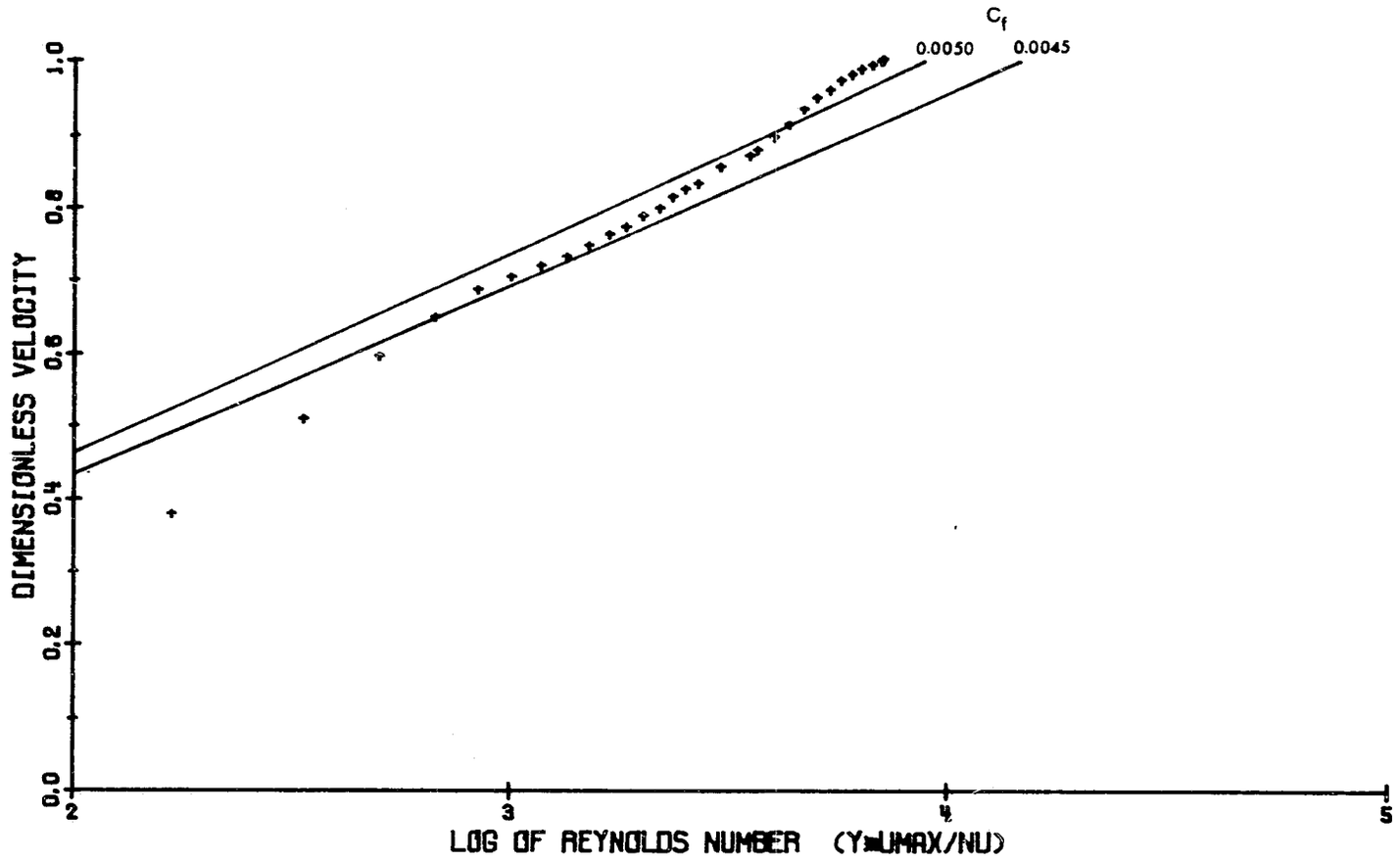

Figure 4

Dimensionless velocity u/U_∞ as a function of log ($y\ U_\infty/\nu$) and lines of constant C_f (from Eq. 6). Test conditions: 1.2% atmospheric pressure, U_∞ = 41.6 m/s, ν = 12.5 cm^2/s, δ = 21.5 cm, and Re_θ = 775. Test conducted in air.

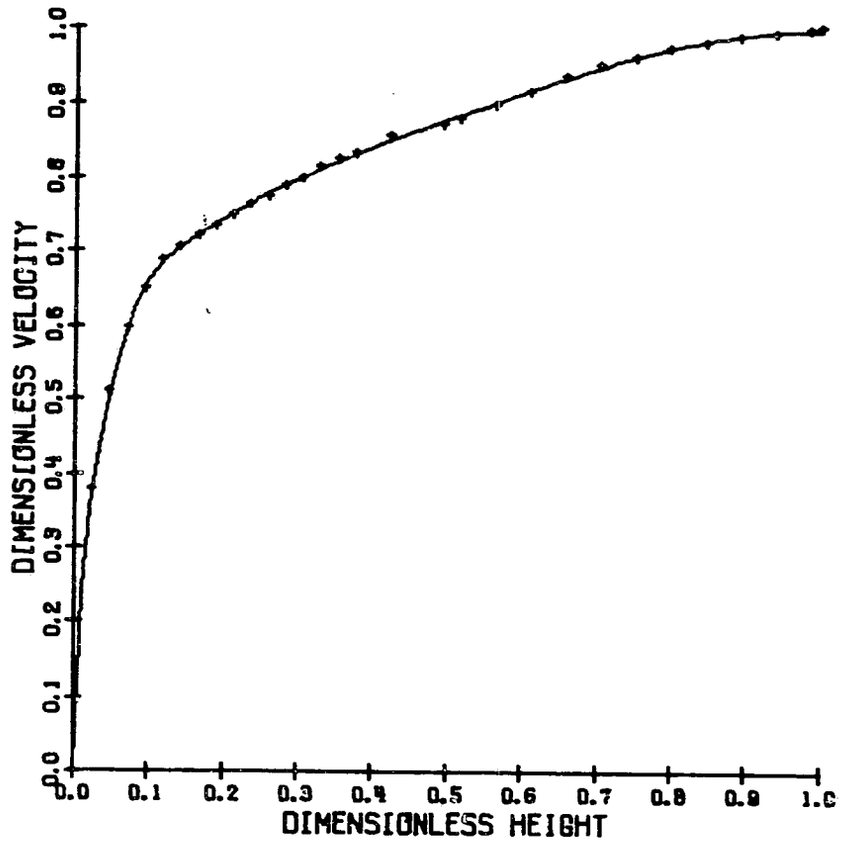

Figure 5

Dimensionless velocity u/U_∞ as a function of y/δ (data points) and the cubic spline curve fit (solid line). Test conditions same as those in Figure 4.

by Simpson (1970) for turbulent boundary layer flows with $Re_\Theta < 6000$ that for the low-Reynolds-number flows, the von Kármán constant κ is replaced by

$$\Omega = 0.40\ (Re_\Theta/6000)^{-1/8} \tag{9}$$

This replacement results in a steepening of the turbulent core region when plotted as u/U_∞ versus log (yU_∞/ν). Huffman and Bradshaw (1972) also disagree with the results of Simpson, and show the validity of the conventional values of the coefficients in the law of the wall for low Reynolds numbers, $1000 < Re_\Theta < 6000$, to be in agreement with the present data.

(iii) $425 < Re_\Theta < 600$. For the lower Reynolds number flows, those in the range $425 < Re_\Theta < 600$, an interesting phenomenon is displayed in some of the profiles. The mean velocity profile of the experimental data no longer correlates with the "universal" velocity profile.

An upper-limit value of the skin-friction coefficient is approximately 0.0048, as determined by Coles (1962) for turbulent boundary layers in a zero-pressure-gradient smooth plate flow. However, for the profiles within this low-Reynolds-number range, the Clauser method consistantly predicts, C_f to be greater than 0.005. This is as much as 15% higher than that found from evaluating the slope of the velocity profile within the viscous region. The disagreement is too great to be dismissed as the accuracy of the methods, and indicates a breakdown of the law of the wall for Reynolds numbers Re_Θ less than 600.

Figure 6 shows a typical velocity profile plot of u/U_∞ versus log (yU_∞/ν) along with the lines representing constant values of C_f. This flow has a Reynolds number based on a momentum-deficit thickness of 510 and a shape factor of 1.47, and was taken at a pressure of 1.6% atmospheric in air. It has a boundary layer thickness of 14.9 cm, a kinematic viscosity of 9.48 cm^2/s, and a free-stream velocity of 28.7 m/s. The turbulent core of the profile is fully developed as evidenced by the linear portion of the profile bounded by the viscous sublayer beneath and the wake region above (Figure 6). In this profile the turbulent core region seems to parallel the lines of constant C_f, as can be seen in the figure. However, the Clauser method predicts, $C_f = 0.0052$, which is in disagreement with that found from the slope of the profile at the wall, and in disagreement with the findings of Coles (1962). Thus, the law-of-the-wall behavior as described in Eq. (5) does not appear to adequately describe the mean velocity profiles in the lower-Reynolds-number, turbulent-boundary-layer flows.

At these lower Reynolds numbers the size of the viscous sublayer increases in relation to the portion of the boundary layer it occupies. This can be seen in the plot of u/U_∞ versus y/δ for the same profile as before, shown in Figure 7. The correlation of the growth of the viscous sublayer with the breakdown of the law of the wall leads to the conclusion that the sublayer grows to heights of approximately 1 cm because the profile cannot withstand the higher surface shear stress.

Another boundary-layer profile from this Reynolds number range is shown in Figure 8, a plot of u/U_∞ versus log (yU_∞/ν). This profile was taken at 0.38% atmospheric pressure in CO_2 and has a Reynolds number $Re_\theta = 579$. It was taken at a free-stream velocity of $U_\infty = 58.0$ m/s, a kinematic viscosity $\nu = 19.8$ cm^2/s, and a boundary layer thickness of 18.0 cm. As can be seen

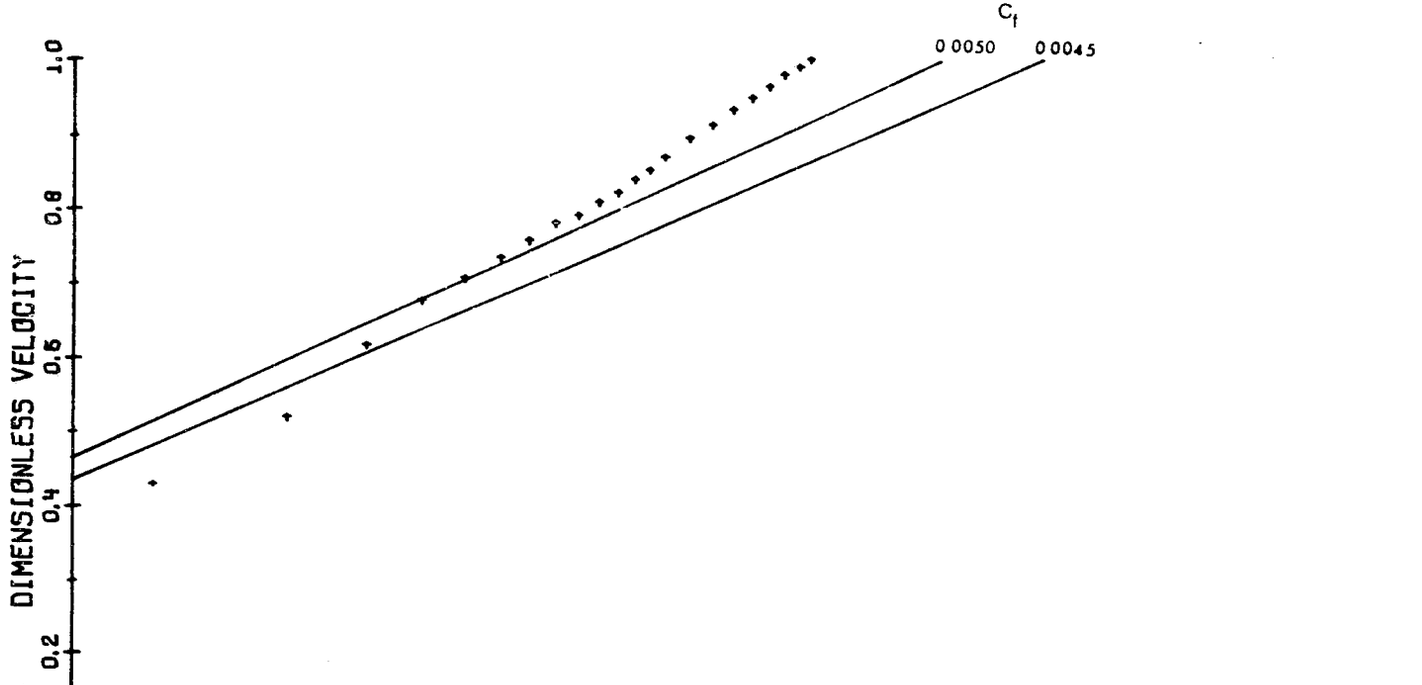

Figure 6

Dimensionless velocity u/U_∞ as a function of log ($y\ U_\infty/\nu$) and lines of constant C_f (from Eq. 6). Test conditions: 1.6% atmospheric pressure, U_∞ = 28.7 m/s, ν = 9.48 cm^2/s, δ = 14.9 cm, and Re_θ = 510. Test conducted in air.

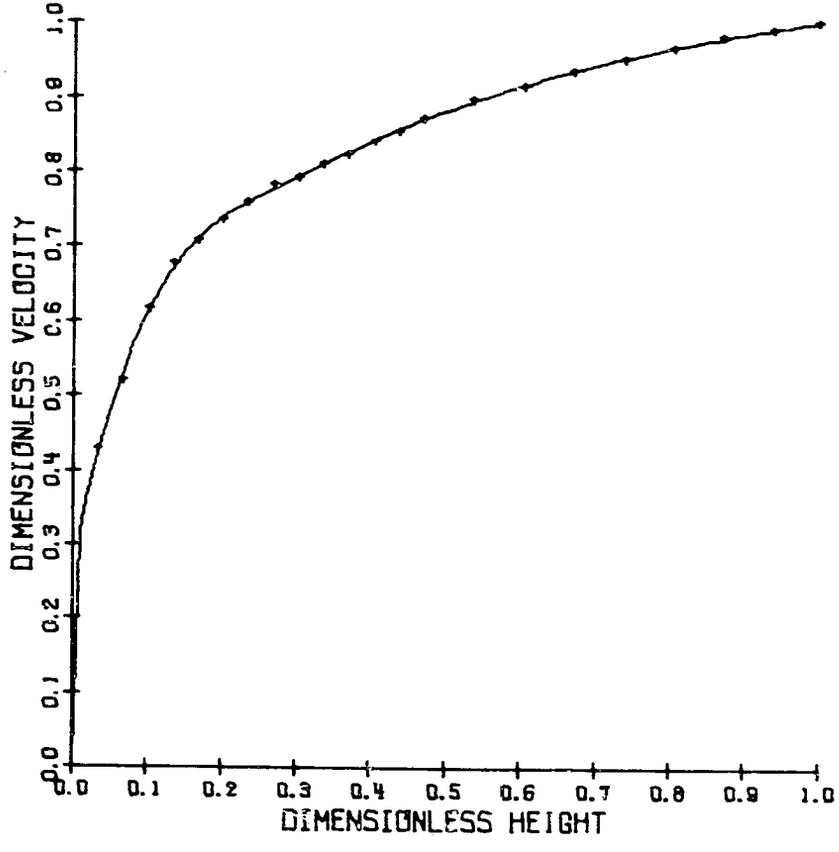

Figure 7

Dimensionless velocity u/U_∞ as a function of y/δ (data points) and the cubic spline curve fit (solid line). Test conditions same as those in Figure 6.

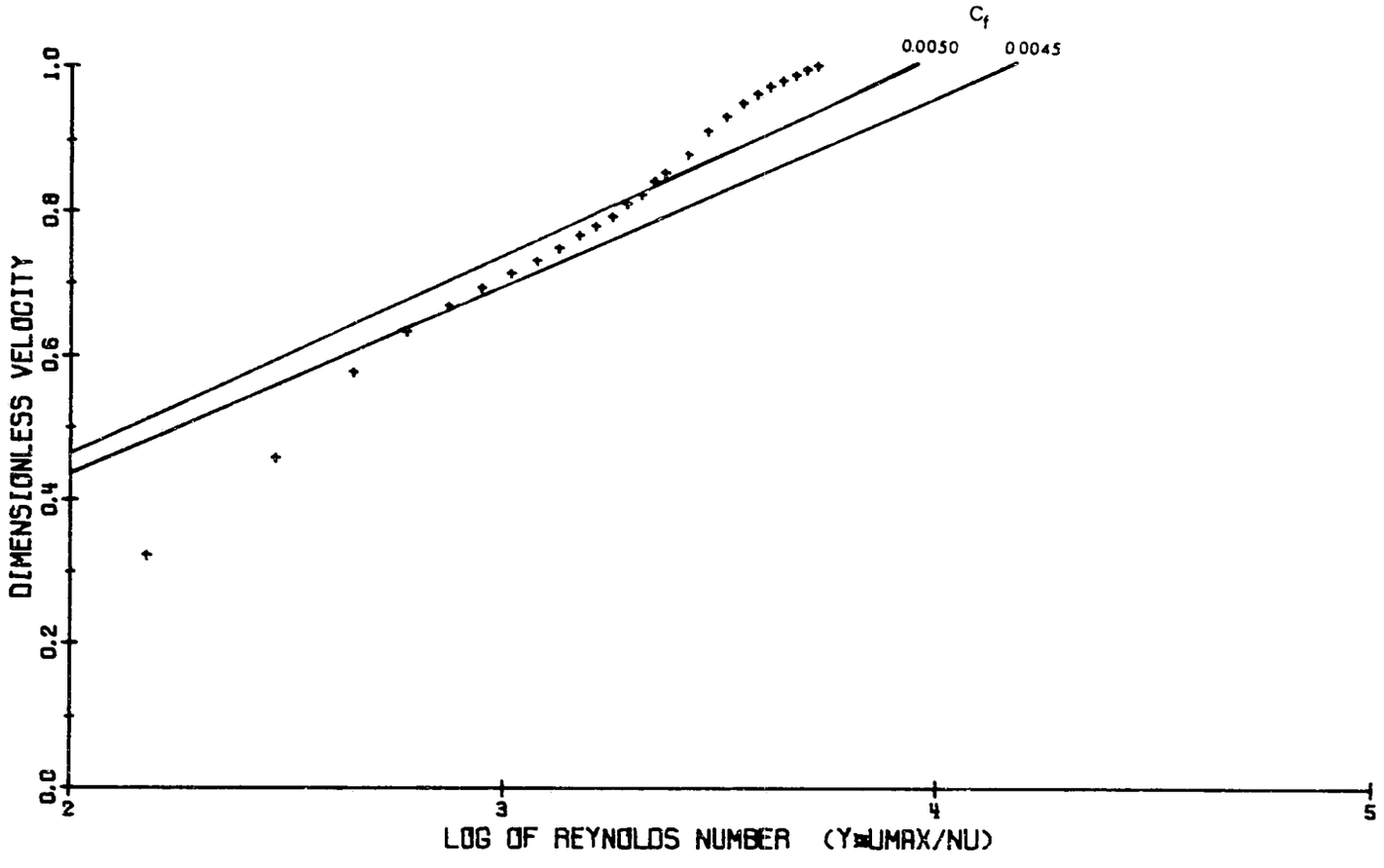

Figure 8

Dimensionless velocity u/U_∞ as a function of log ($y\ U_\infty/\nu$) and lines of constant C_f (from Eq. 6). Test conditions: 0.39% atmospheric pressure, U_∞ = 58.0 m/s, ν = 19.8 cm^2/s δ = 18.0 cm, and Re_θ = 579. Test conducted in CO_2.

from the figure the turbulent core region cuts across the lines of constant C_f. The slope of this linear region is larger than that predicted by the law of the wall. Other profiles within this Reynolds number range also displays this behavior. The law-of-the-wall formulation can be extended to model these flows by changing the values of the constants κ and B to be functions of the Reynolds number Re_θ, an idea similar to that proposed by Simpson for $Re_\theta < 6000$. However, in the present study these are only observed for $Re_\theta < 600$.

Figure 9 shows the same velocity profile plotted as u/U_∞ versus y/δ. The large size of the viscous sublayer is clearly shown, extending to y/δ = 0.1 which is much larger than that found in higher Reynolds number flows.

These results are in agreement with similar findings. Others have observed the breakdown in the law of the wall and the growth of the viscous sublayer in pipe and channel flow, including Patel and Head(1969), Beavers, et al. (1971), and Kudva and Sesonke (1972).

(iv) $200 < Re_\theta < 425$. These flows, though appearing to be laminar, display many turbulent wake features. They are in the transitional range since they have no mature turbulent core region.

The separate boundary layer profiles within this range occur at various values of Re_θ occuring in the transition region. The first sign of deviation from the laminar profile is shown in Figure 10 for Re_θ = 253, which displays the effects of a turbulent wake region. Note that the wall region is still linear, nearly unaffected by this change. This turbulent wake region becomes more dominant as the Reynolds number increases, and leads to the development of the turbulent core. Figures 11 and 12 show profiles at Re_θ = 325 and 401, respectively, and include the familiar laminar profile

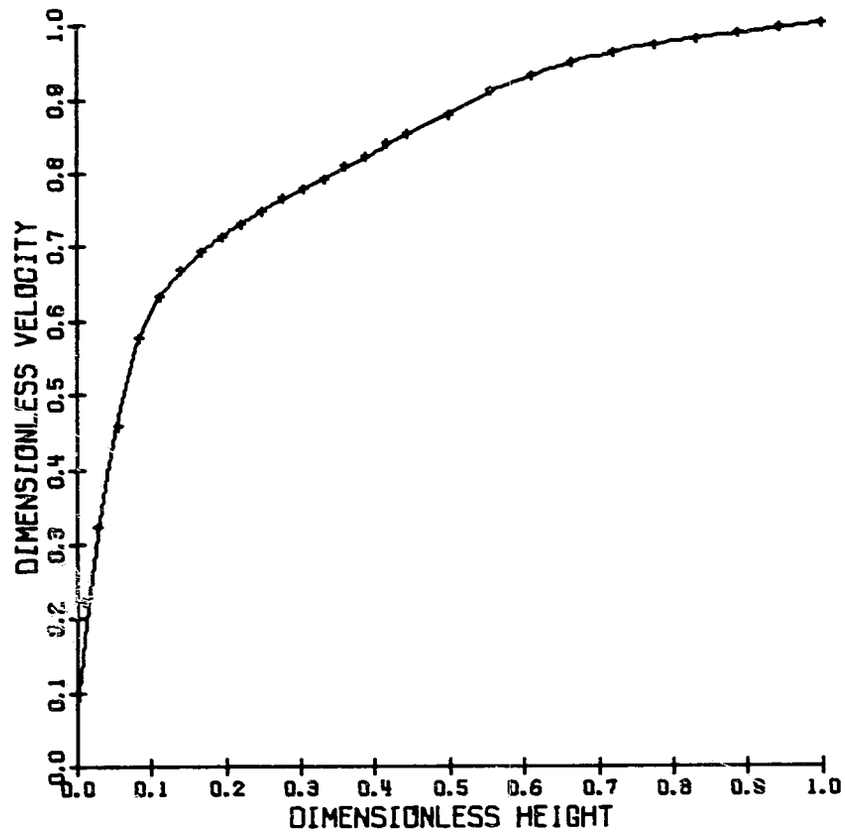

Figure 9

Dimensionless velocity u/U_∞ as a function of y/δ (data points) and the cubic spline curve fit (solid line). Test conditions same as those in Figure 8.

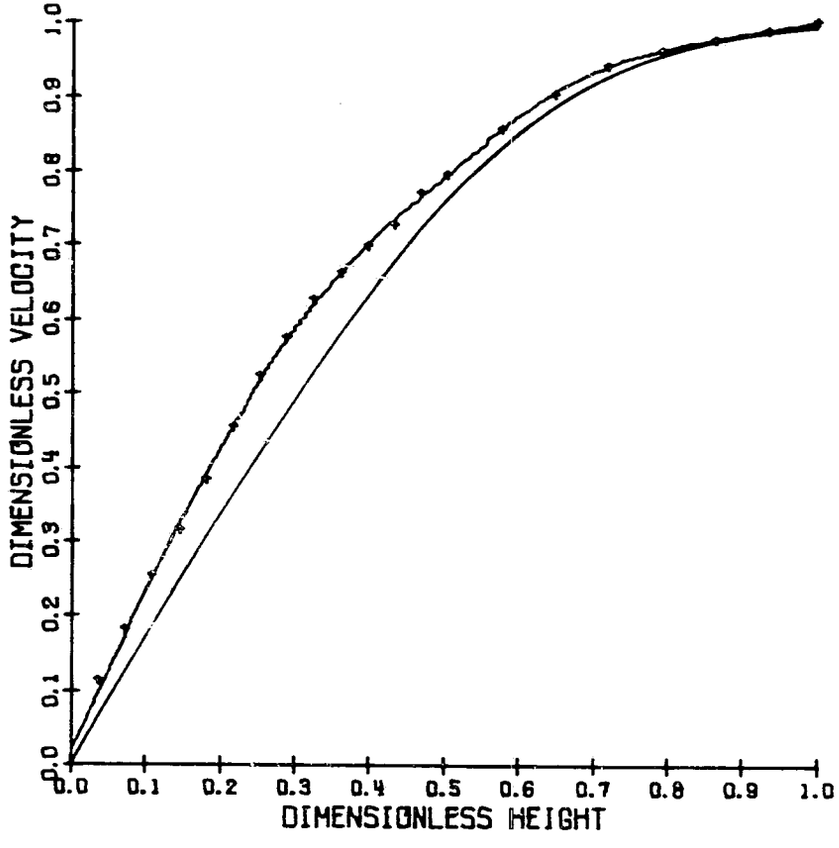

Figure 10

Dimensionless velocity u/U_∞ as a function of y/δ (data points) and the cubic spline curve fit (corresponding solid line). Also shown is the laminar profile as determined by Blasius. Test conditions: 0.39% atmospheric pressure, U_∞ = 67.9 m/s, ν = 48.5 cm^2/s, δ = 13.9 cm, and Re_θ = 253. Test conducted in air.

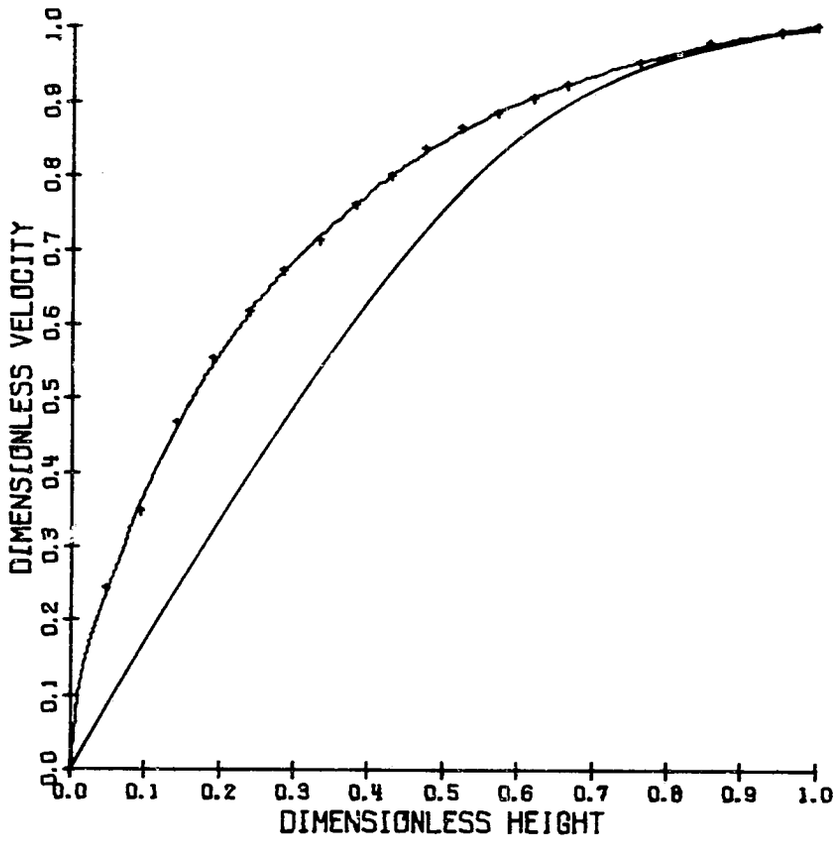

Figure 11

Dimensionless velocity u/U_∞ as a function of y/δ (data points) and the cubic spline curve fit (corresponding solid line). Also shown is the laminar profile as determined by Blasius. Test conditions: 0.39% atmospheric pressure, U_∞ = 98.0 m/s, ν = 39.9 cm^2/s, δ = 10.5 cm, and Re_θ = 325. Test conducted in air.

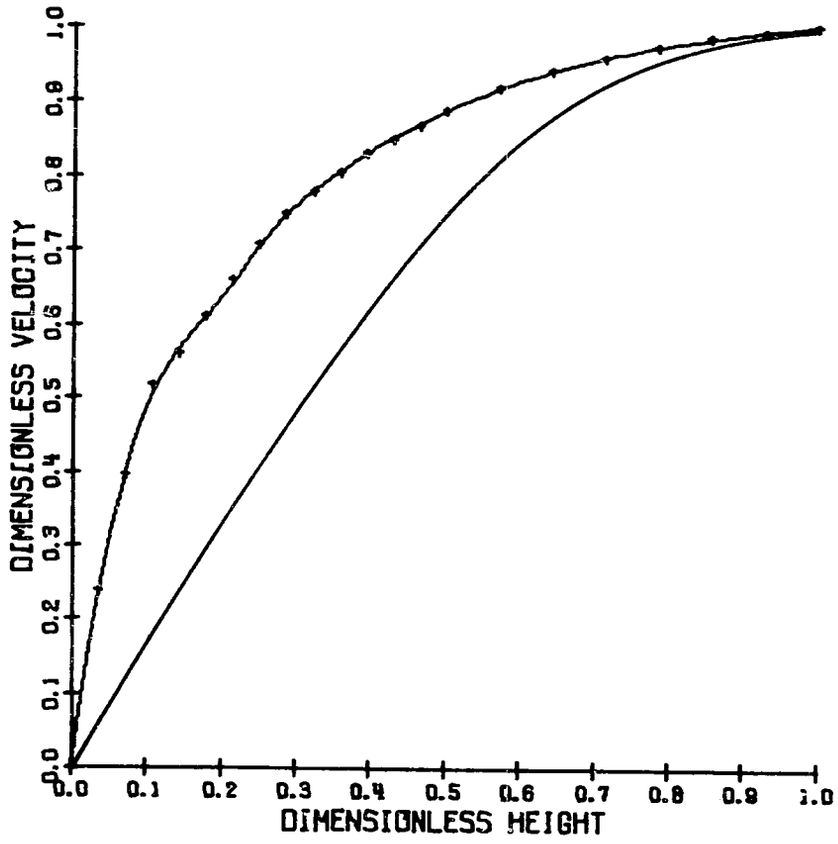

Figure 12

Dimensionless velocity u/U_∞ as a function of y/δ (data points) and the cubic spline curve fit (corresponding solid line). Also shown is the laminar profile as determined by Blasius. Test conditions: 0.42% atmospheric pressure, U_∞ = 96.0 m/s, ν = 37.1 cm^2/s, δ = 14.1 cm, and Re_θ = 401. Test conducted in air.

developed by Blasius for comparison. The linear wall region is still present although it no longer reaches as far into the profile and has a steeper gradient at the wall for the higher Reynolds numbers. This linear region transforms into the large viscous sublayer observed in the range $425 < Re_\Theta < 600$ where the turbulent core region is fully developed.

Calculation of C_f for $600 < Re_\Theta < 2000$

Table 1 presents a summary of the present boundary layer data. These data represent 15% of all that were taken. The data in Table 1 are a select group. Of the data taken, certain profiles were selected to be analyzed because of their stable background conditions (constant ambient pressures and free-stream velocities) as well as having well-defined mean velocity profiles. Then the data were narrowed down to include only those runs where C_f values were well defined by the Clauser method.

The table, listing the profiles by Reynolds numbers based on momentum-deficit thickness, includes the values of skin-friction coefficient found by the Clauser method, along with those calculated from the expressions by White, Ludwieg & Tillmann, and the 1/7th-power law (see Appendix A). Plots comparing the data with each of these methods are shown in Figures 13 - 15. The 1/7th-power-law formulation, shown as the solid line in Figure 13, tends to predict a value of C_f higher than that found by the Clauser method. The curve matches the general trend of the data and is a fair predictor for this Reynolds number range, although the values are consistantly higher than the experimentally determined values. The expression by Ludwieg & Tillmann contains a dependence on the shape factor. In Figure 14 the three lines represent constant values of H. These are the minimum, mean, and maximum

TABLE 1-A

FLOW CONDITIONS AND SKIN FRICTION COEFFICIENTS FOR EXPERIMENTAL DATA

Run Number	Re_θ	H_0 (% atm)	δ (cm)	U_∞ (m/s)	ν (cm^2/s)	k^+	H	$C_f \times 1000$ a	b	c	d	e
1*	644	0.68	19.5	32.7	11.5	0.84	1.45	4.80	5.08	4.49	4.51	4.90
2*	655	0.30	15.8	96.2	26.8	1.05	1.48	4.81	5.06	4.32	4.33	4.88
3*	741	1.0	19.5	28.3	7.74	1.08	1.45	4.81	4.91	4.37	4.35	4.73
4*	768	0.39	16.7	85.1	20.3	1.24	1.47	4.81	4.86	4.18	4.15	4.69
5	775	1.2	21.3	41.6	12.5	0.97	1.46	4.67	4.85	4.24	4.21	4.68
6*	795	0.38	17.0	91.8	21.5	1.25	1.40	4.75	4.82	4.65	4.64	4.65
7*	935	0.43	18.5	86.6	18.8	1.30	1.49	4.43	4.63	3.84	3.75	4.47
8*	976	0.39	18.5	97.5	20.8	1.33	1.38	4.50	4.58	4.54	4.49	4.42
9*	982	2.0	18.5	17.6	3.88	1.30	1.37	4.55	4.57	4.58	4.57	4.41
10*	1020	0.64	18.0	61.0	11.7	1.49	1.47	4.50	4.53	3.87	3.78	4.38
11*	1020	0.59	17.5	70.2	13.3	1.49	1.45	4.44	4.53	4.00	3.92	4.37
12	1030	2.6	18.9	24.0	5.36	1.24	1.49	4.24	4.52	3.76	3.66	4.37
13*	1030	0.46	19.0	88.0	17.6	1.41	1.49	4.40	4.52	3.76	3.66	4.36
14	1060	3.9	17.2	20.7	3.88	1.48	1.45	4.31	4.49	3.94	3.85	4.33
15	1090	3.9	18.1	20.7	3.88	1.48	1.43	4.27	4.45	4.07	3.99	4.30
16	1160	1.9	18.2	47.5	8.17	1.60	1.36	4.18	4.39	4.44	4.36	4.23
17	1160	8.3	17.5	10.6	1.88	1.55	1.42	4.05	4.38	4.02	3.92	4.23
18	1180	1.6	20.5	47.6	9.03	1.45	1.44	4.20	4.37	3.94	3.83	4.22
19*	1200	0.62	21.5	70.5	12.8	1.53	1.47	4.20	4.35	3.71	3.60	4.20
20*	1240	2.0	22.0	20.9	3.89	1.49	1.40	4.24	4.31	4.11	4.01	4.16
21	1250	2.0	19.0	43.3	7.51	1.55	1.45	4.00	4.31	3.78	3.67	4.16

* Indicates CO_2; otherwise the fluid is air

[a] Skin-friction coefficient as determined from the Clauser Method

[b] Skin-friction coefficient as calculated from the 1/7th-power law formulation (Eq. A-1)

[c] Skin-friction coefficient as calculated from the relation by Ludwieg & Tillmann (Eq. A-2)

[d] Skin-friction coefficient as calculated from the relation by White (Eq. A-3)

[e] Skin-friction coefficient as calculated from Eq. 13

TABLE 1-A (Continued)

Run Number	Re_θ	H_0 (% atm)	δ (cm)	U_∞ (m/s)	ν (cm^2/s)	k+	H	C_f x 1000 a	b	c	d	e
22*	1320	0.74	19.5	60.1	10.2	1.59	1.43	4.04	4.24	3.81	3.70	4.10
23	1400	7.5	16.8	14.7	2.07	1.91	1.43	4.00	4.18	3.77	3.65	4.04
24*	1450	0.66	22.0	71.4	12.0	1.61	1.38	3.99	4.15	4.07	3.96	4.01
25	1470	2.6	20.4	36.7	5.48	1.82	1.40	4.10	4.14	3.95	3.84	4.00
26	1500	2.6	19.5	36.6	5.48	1.76	1.43	3.87	4.11	3.71	3.58	3.97
27*	1540	0.71	22.5	69.1	11.1	1.66	1.40	3.94	3.74	4.09	3.81	3.95
28*	1600	1.1	19.0	54.8	7.59	1.94	1.36	4.02	4.05	4.10	3.99	3.91
29*	1690	1.7	17.5	34.9	4.17	2.19	1.41	3.80	4.00	3.69	3.56	3.86
30	1780	1.5	16.9	90.0	10.4	2.23	1.39	3.68	3.94	3.77	3.64	3.81
31*	1840	1.7	18.5	36.1	4.17	2.24	1.42	3.71	3.91	3.60	3.47	3.78
32	1940	2.1	18.0	68.6	7.49	2.34	1.48	3.60	3.86	3.21	3.06	3.73
33	1940	11.	18.6	12.8	1.40	2.35	1.37	3.67	3.86	3.79	3.67	3.73
34*	1970	6.4	18.0	10.2	1.17	2.20	1.40	3.54	3.84	3.61	3.48	3.72
35*	2100	2.1	19.0	36.9	3.73	2.51	1.40	3.58	3.78	3.58	3.45	3.66
36	2240	5.9	18.5	24.8	2.37	2.64	1.40	3.52	3.72	3.49	3.35	3.60
37*	2470	5.4	19.6	14.2	1.35	2.64	1.39	3.50	3.63	3.46	3.33	3.51
38	2490	7.6	16.4	24.9	2.02	3.03	1.45	3.38	3.62	3.15	3.01	3.51
39*	3220	5.0	18.2	22.1	1.48	3.73	1.37	3.46	3.40	3.35	3.23	3.29
40	3250	6.4	16.5	43.0	2.42	4.36	1.45	3.35	3.39	2.94	2.80	3.28
41	3800	47.	16.3	6.51	0.328	4.81	1.37	3.26	3.26	3.18	3.06	3.16
42	4490	22.	17.7	16.2	0.716	5.20	1.44	2.93	3.13	2.73	2.61	3.03
43	5020	100.	15.1	4.16	0.155	6.29	1.40	3.05	3.04	2.81	2.70	2.95
44	6270	21.	17.6	23.3	0.732	7.12	1.38	2.78	2.88	2.75	2.66	2.79
45	7010	49.	17.7	11.1	0.320	7.66	1.39	2.71	2.80	2.62	2.54	2.72

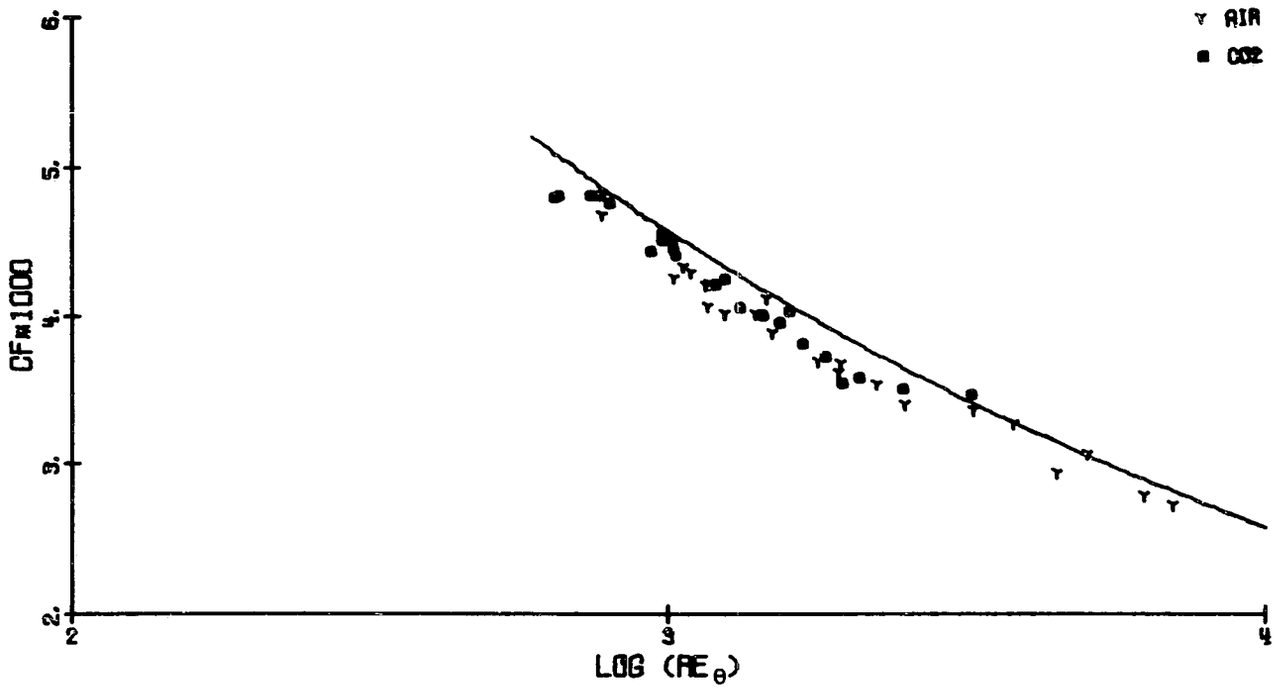

Figure 13

Comparison of the data with the 1/7th-power-law relation for the skin-friction coefficient (Eq. A-1).

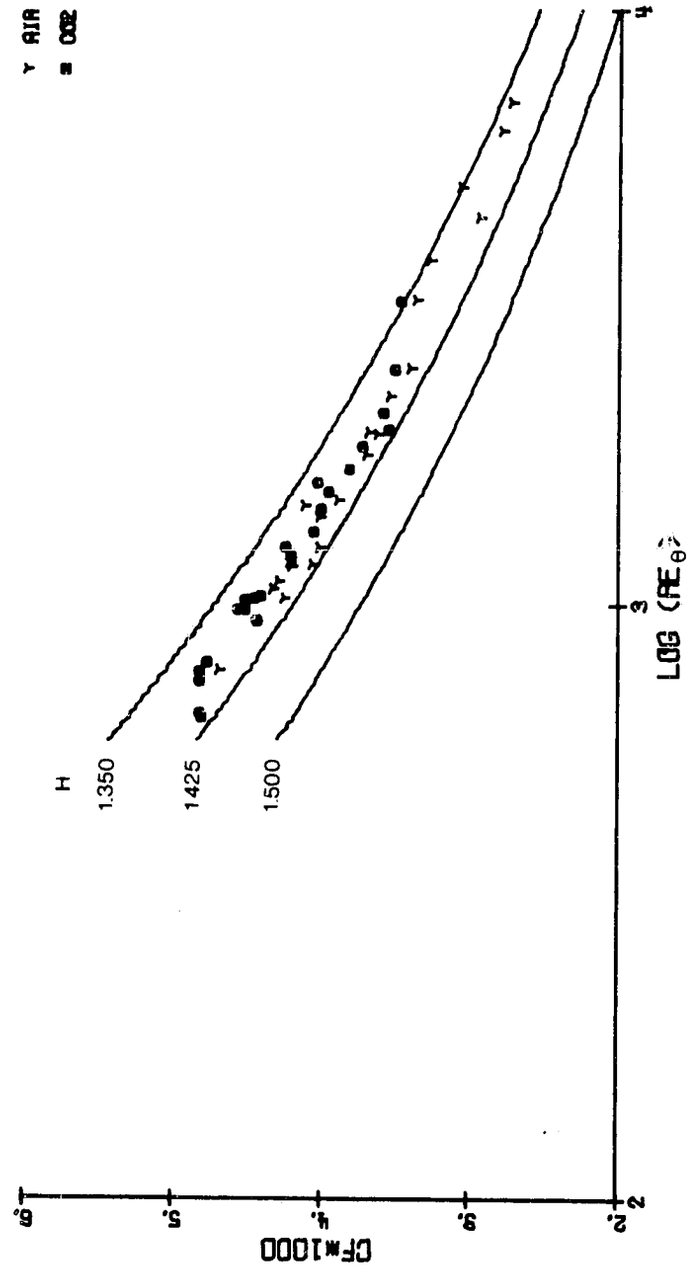

Figure 14

Comparison of the data with the expression by Ludwieg & Tillmann for the skin-friction coefficient (Eq. A-2). Each line represents a constant value of the shape factor.

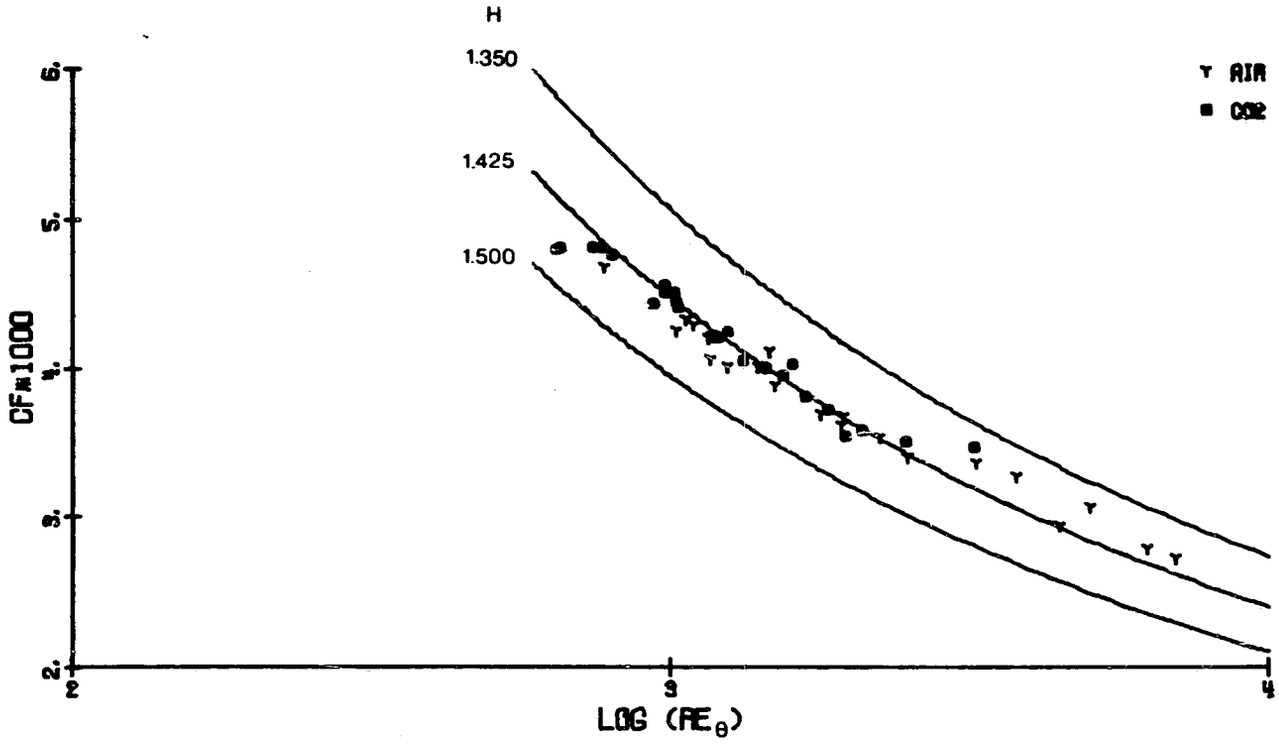

Figure 15

Comparison of the data with the expression by White for the skin-friction coefficient (Eq. A-3). Each line represents a constant value of shape factor.

values for the data. If this expression were to represent the data accurately, the points would straddle the center curve and be bound by the two outer curves. However, the data tend to cluster on one curve, showing little variation with shape factor. It can be seen from the figure that this prediction method results in a low estimate for the skin-fricton coefficient. The expression developed by White also contains a dependence on the shape factor. This expression is displayed in Figure 15 for the above-mentioned values of H. White's prediction method results in values of C_f which are, in general, lower than the values predicted by the Clauser method.

The equations developed by both White and Ludwieg and Tillmann are based on data for Reynolds numbers Re_θ as low as 1000. Although it is believed that the data presented in this paper should be more accurate than previous data, it is expected that these data should blend with other accepted expressions at the higher Reynolds numbers. From Figures 13-15 this appears to be true. For Re_θ ranging between 600 and 2000, it can be seen that the aforementioned expressions tend to predict a C_f systematically different than the values found by the Clauser method. The 1/7th-power-law relation predicts a consistently high value, whereas the approximations by Ludwieg and Tillman and by White tend to predict C_f somewhat low. This disagreement among these widely used expressions confirms the lack of reliability they offer in the low-Reynolds-number range.

An expression was developed to be accurate exclusively in the range of this data. A basic form of an equation which would describe the data was assumed. This form, which accounts for C_f dependence on Reynolds number Re_θ as well as shape factor H, thus allowing for effects due to pressure gradients, is

$$C_f = (10^{A_2} \, Re_\theta^{\,A_3})^{H^{A_1}} \quad . \tag{10}$$

It can be manipulated into a form which is easy to use in making curve fits. Upon taking logarithms of both sides and then combining the shape factor term with the skin-friction, this becomes

$$H^{-A_1} \log_{10} (C_f) = A_2 + A_3 \log_{10} (Re_\theta) \; . \tag{11}$$

Thus, by assuming a value of A_1, the curve fit becomes a very simple linear least-squares curve fit, as shown in Figure 16 for $A_1 = 0$.

Various fits were computed for different values of A_1. An expression to measure the accuracy of each fit was developed in order to compare the curve fits resulting from the assumed values of A_1. This expression is a measure of the normalized error, weighting the errors at the lower C_f's as much as those at the higher values, and has the form

$$E_s = \sum_{i=1}^{n} \left(\frac{C_f \text{ (exact)} - C_f \text{ (predicted)}}{C_f \text{ (exact)}} \right)^2 \quad 1/2 \; , \tag{12}$$

where in this case, n is the number of data points, C_f (predicted) is found from Eq. (10) using the computed values of A_2 and A_3 and the assumed value of A_1, and C_f (exact) is the value determined by the Clauser method. The error was defined so that all E_s's may be directly compared for various methods of predicting C_f. The results of curve fits for several different values of A_1 are listed in Table 2. A comparison of the error for different values shows that the best curve fit, that having the minimum error, results when $A_1 = 0$. This implies that for this narrow range of data there appears

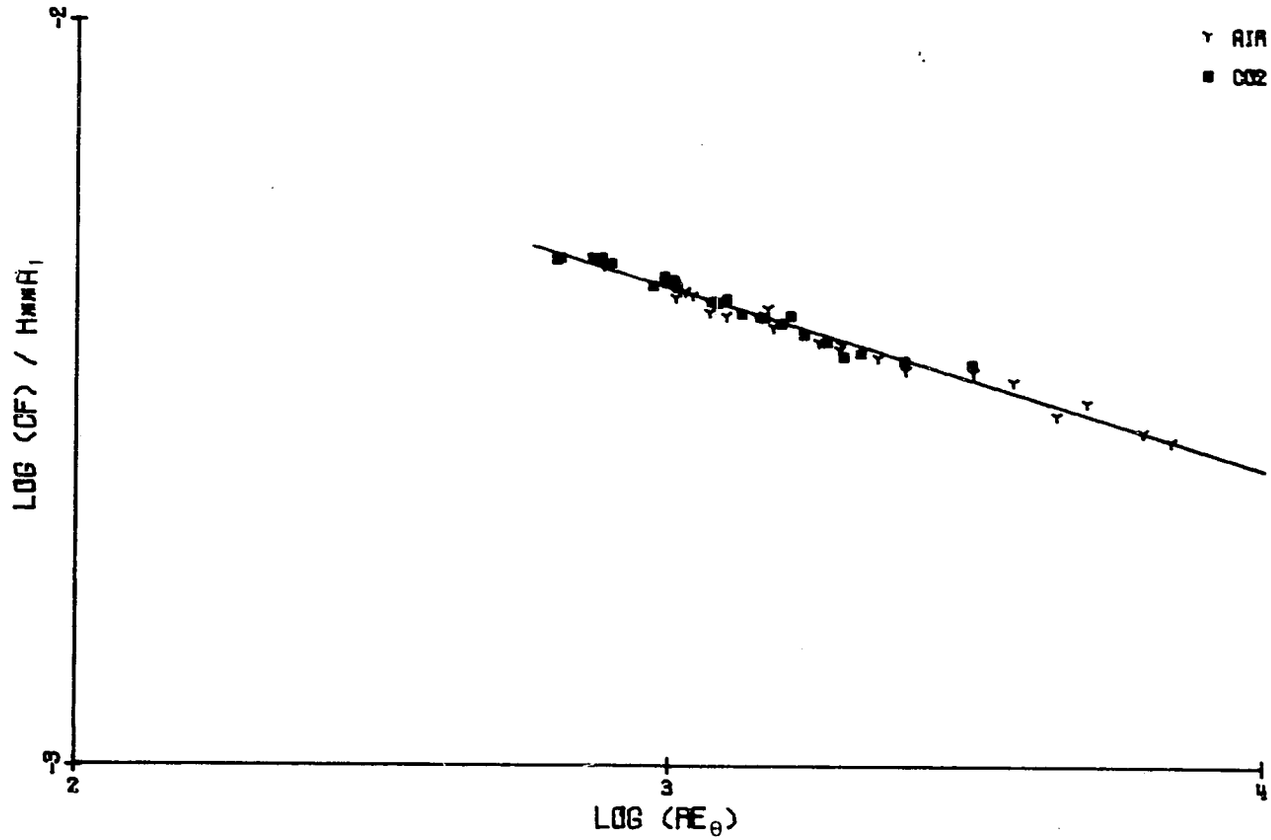

Figure 16

Logarithmic plot of C_f as a function of Re_θ showing the linear least squares curve fit for $A_1 = 0$ in Eq. (11).

TABLE 2

COEFFICIENTS FOR EQ. (10) ASSUMING VARIOUS VALUES OF A_1

A_1	A_2	A_3	Es x 10^5 (Eq. 12)
0.20	-1.44	-0.251	27.3
0.10	-1.53	-0.249	12.6
0.05	-1.57	-0.248	6.18
0.02	-1.60	-0.248	2.71
0.01	-1.61	-0.247	1.78
0.00	-1.62	-0.247	1.37
-0.01	-1.63	-0.247	1.81
-0.02	-1.63	-0.247	2.70
-0.05	-1.66	-0.246	5.79
-0.10	-1.71	-0.245	10.9
-0.20	-1.81	-0.242	19.9

to be no correlation of shape factor with skin-friction at low Reynolds numbers. This somewhat surprising result can be attributed to the fairly small range of H in this data set, ranging from 1.35 to 1.50, along with the lack of sufficient data throughout the Reynolds number range covering the shape factor range. However, these low-Reynolds-number flows only seem to occur in the limited range of shape factors for $Re_\Theta < 2000$.

The final expression was found by setting $A_1 = 0$, eliminating the shape factor dependence from the prediction of C_f. This final expression is

$$C_f = 0.0242\ Re_\Theta^{-0.247} \tag{13}$$

and is displayed in Figure 17 along with the data. It is very similar to the relationship derived by the 1/7th-power law developed in Schlichting (1968) for a smooth flat plate, which is

$$C_f = 0.0256\ Re_\Theta^{-1/4} \quad . \tag{14}$$

However, a comparison of Figures 13 and 17 shows that Eq. (13) is a better predictor of the skin-friction factor. The 1/7th-power-law formula predicts a systematically high value for C_f. A comparison of the accuracy of this new expression to others commonly used is shown in Table 3. The normalized errors were computed using profiles with $Re_\Theta > 600$. Using Eq. (12), the Clauser value of C_f was compared with that predicted by each method. All error values are computed using the previous error expression for the various predicting methods compared with the values found by the Clauser method. This curve fit tends to blend with the expression from White for a shape factor equal to the average of the data as Re_Θ takes on values greater than 2000. This empirical equation should only be used in the low-reynolds-number range,

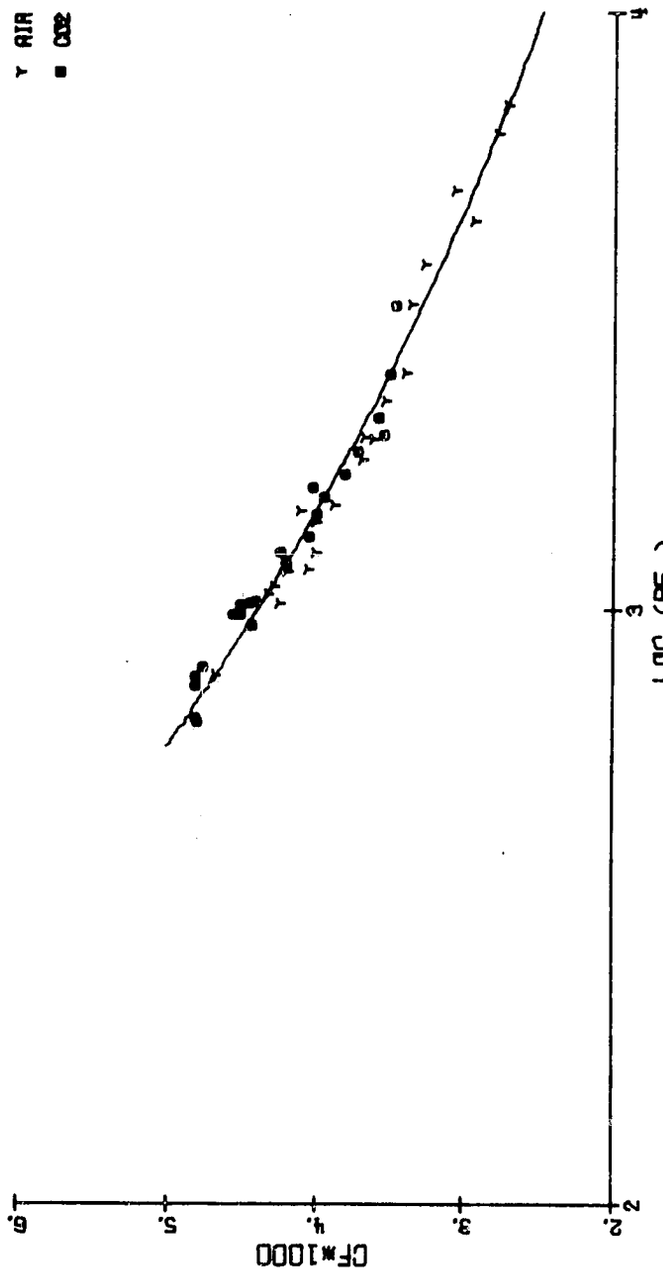

Figure 17
Comparison of the data with Eq. (13).

TABLE 3

COMPARISON OF THE ACCURACY OF VARIOUS APPROXIMATE EXPRESSIONS FOR C_f OVER THE RANGE $600 < Re_\theta < 7000$

Expression	Es x 1000 (Eq. 12)
Eq. (13)	3.54
1/7th-power law (Eq. A-1)	6.89
Ludwieg and Tillmann (Eq. A-2)†	10.6
White (Eq. A-3)†	13.4

†Note that these equations were developed for $Re_\theta > 1000$ and have been extrapolated down to $Re_\theta = 600$.

for $600 < Re_\theta < 2000$, for smooth-flat-plate flows in zero-pressure-gradient, turbulent boundary layers.

Relating C_f To Re_x

Another method of comparison of these data with other expressions is to relate the skin-friction coefficient to the Reynolds number based on downstream distance, $Re_x = x\, U_\infty/\nu$. Although every profile was obtained at the same downstream distance in the tunnel, x = 6.36 m, there is enough variety in the free-stream velocities and kinematic viscosities for this approach to cover a wide range of Reynolds numbers Re_x. Again excluding all data where the boundary layer does not obey the law of the wall, $Re_\theta < 600$; this represents a range of Re_x from 181,000 to 2,210,000. Figure 18 is a plot of C_f verses Re_x. The solid line represents the expression derived by Schultz-Grunow as presented in Schlichting (1968):

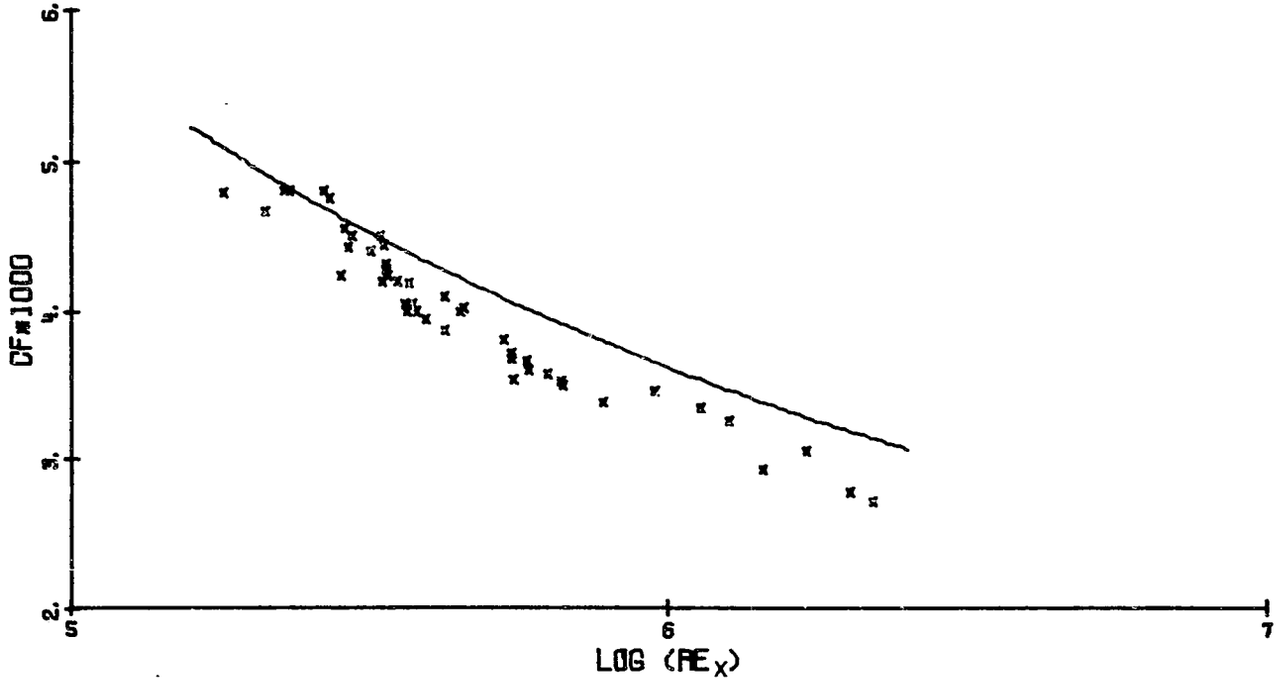

Figure 18

Comparison of the data with the expression by Schultz - Grunow based on Re_x (Eq. 15).

$$C_f = 0.370 \ (\log_{10} Re_x)^{-2.584} \ . \qquad (15)$$

As can be seen from the figure, this expression predicts C_f continuously higher than the "exact" values.

In order to increase the accuracy of this predicting method over the narrow range of Reynolds numbers, the coefficients in Eq. (15) were adjusted. The data were fitted to an expression of the form

$$C_f = B_1 \ (\log_{10} Re_x)^{B1} \ . \qquad (16)$$

This equation reduces to a simple linear expression upon taking logarithms of both sides:

$$\log_{10} C_f = \log_{10} B_1 + B_2 \log_{10} (\log_{10} Re_x) \ . \qquad (17)$$

These values of B_1 and B_2 were found from a linear least-squares curve fit of the data. The curve fitting resulted in the final expression:

$$C_f = 0.987 \ (\log_{10} Re_x)^{-3.19} \ . \qquad (18)$$

This approximation is displayed in Figure 19 along with the data. The corresponding value of Re_x for each data point is listed in Table 4, along with the values of C_f found by the Clauser method, the expression by Schultz-Grunow and (Eq. 18). A comparison of the error of both equations as computed from Eq. (12) using the "exact" Clauser values and the values predicted by Eqs. (15) and (18) is presented in Table 5. It is seen that an adjustment to the coefficients found by Schultz-Grunow is necessary to increase the accuracy of the prediction over the range of this data. This expression is useful for estimating the skin-friction coefficient from a flow where only the free-stream properties are known. This would be a good estimator to use during wind-tunnel testing, a situation where the velocity distribution is not available.

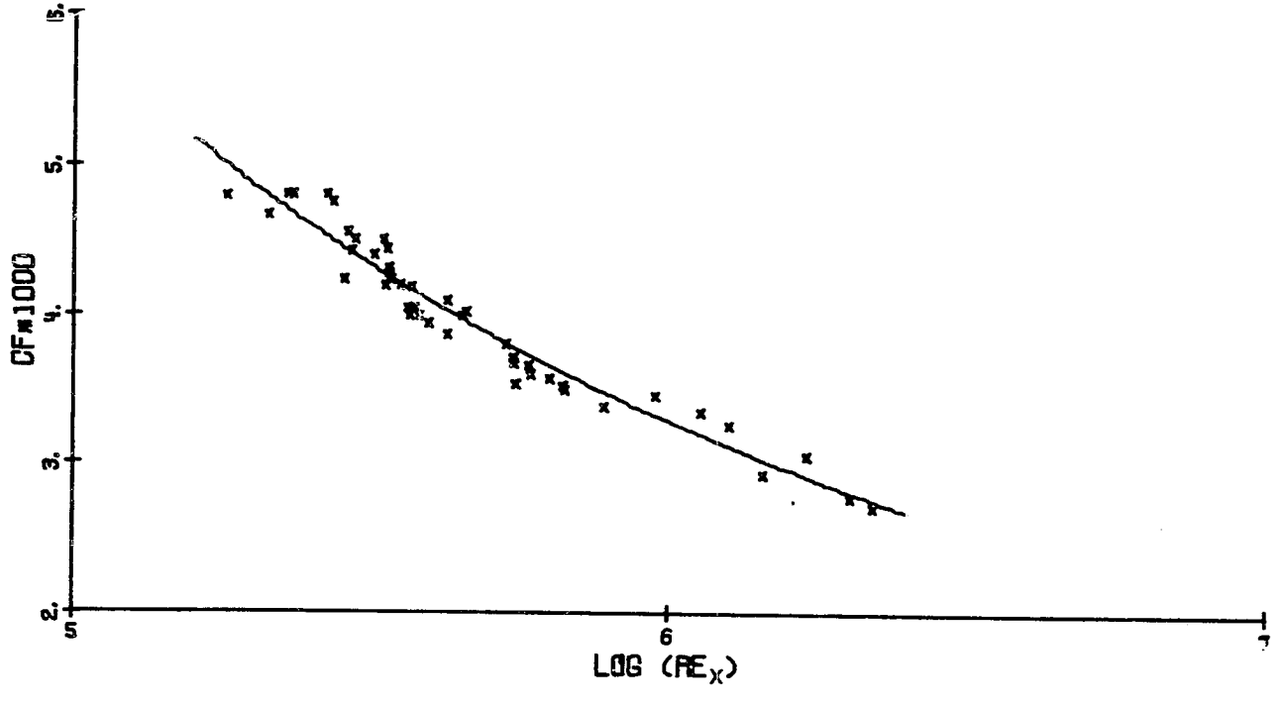

Figure 19

Comparison of the data with Eq. (18) for the prediction of C_f based on Re_x.

TABLE 4

COMPARISON OF SKIN FRICTION PREDICTIONS BASED ON Re_x

Run Number	Re_x x10-3	C_f x 1000 a	b	c
1	181.	4.80	5.08	4.95
2	228.	4.81	4.84	4.66
3	233.	4.81	4.81	4.64
4	267.	4.81	4.68	4.48
5	212.	4.67	4.91	4.75
6	272.	4.75	4.66	4.46
7	293.	4.43	4.59	4.37
8	298.	4.50	4.57	4.36
9	288.	4.55	4.61	4.36
10	332.	4.50	4.48	4.24
11	336.	4.44	4.46	4.23
12	285.	4.24	4.62	4.41
13	319.	4.40	4.51	4.28
14	339.	4.31	4.46	4.22
15	339.	4.27	4.46	4.22
16	370.	4.18	4.38	4.13
17	364.	4.05	4.39	4.14
18	335.	4.20	4.47	4.23
19	353.	4.20	4.42	4.17
20	342.	4.24	4.45	4.21
21	367.	4.00	4.39	4.13
22	375.	4.04	4.37	4.11
23	452.	4.00	4.21	3.93
24	382.	3.99	4.35	4.09
25	426.	4.10	4.26	3.98

[a] Skin-friction coefficient as determined from the Clauser method

[b] Skin-friction coefficient as calculated from the Schultz-Grunow expression (Eq. 15)

[c] Skin-friction coefficient as calculated from Eq. (18)

TABLE 4
(con't)

Run Number	Re_x x10-3	C_f x 1000 a	b	c
26	424.	3.87	4.26	3.99
27	396.	3.94	4.32	4.06
28	459.	4.02	4.19	3.91
29	532.	3.80	4.07	3.77
30	5[illegible].	3.68	4.05	3.74
31	[illegible]1.	3.71	4.05	3.74
32	585.	3.60	4.00	3.69
33	581.	3.67	4.00	3.69
34	554.	3.54	4.04	3.74
35	629.	3.58	3.94	3.62
36	666.	3.52	3.90	3.58
37	669.	3.50	3.90	3.57
38	780.	3.38	3.78	3.44
39	950.	3.46	3.64	3.29
40	1130.	3.35	3.53	3.16
41	1260.	3.26	3.46	3.08
42	1440.	2.93	3.38	2.99
43	1710.	3.05	3.27	2.88
44	2020.	2.78	3.17	2.77
45	2210.	2.71	3.13	272

TABLE 5

COMPARISON OF APPROXIMATE EXPRESSIONS FOR C_f BASED ON Re_x

Expression	Es x 1000 (Eq. 12)
Eq. (18)	4.75
Schultz - Grunow (Eq. 15)	11.8

Comparison of Profiles Obtained in Air and CO_2

Approximately half of the profiles analyzed were obtained in CO_2, the other half in air. As can be seen in Figure 17, neither shows differing behavior. The clustering of the air and CO_2 data points within certain Reynolds number regions is a result of the similarity of the conditions for runs taken on the same day. It does not indicate behavioral trends which depend on the fluid. This should simplify the modeling of the Martian atmosphere within the laboratories on Earth.

Conclusion

A series of boundary layer profiles was obtained at low Reynolds numbers in a low-pressure environmental wind tunnel. These profiles are expected to be extremely accurate as a result of the large boundary layer heights, ranging from 17 to 21 cm. The profiles obtained for $Re_\theta > 2000$ blend well with other existing data, verifying the reliability of the tunnel.

A computer program was developed to analyze a general velocity profile computed from pressure differentials, including the determination of the displacement and momentum-deficit thicknesses. This program greatly reduced the work load in the analysis of over 60 profiles.

The data, covering the range $200 < Re_\theta < 7000$, provide insight into the nature of transitional flows. There appears to be a well-ordered evolutionary process from the laminar to the turbulent profiles. These profiles clearly display the development of the turbulent core region and the shrinking of the laminar sublayer with increasing values of Re_θ.

The fully developed boundary layers are found to occur at Reynolds numbers Re_θ greater than 600. This range is well represented in the data, composing 75% of all the data analyzed, and confirms the law-of-the-wall behavior at these low Reynolds numbers. Calculated values of the skin-friction coefficient from relations by White (1974), Ludwieg and Tillmann (1950), and the 1/7th-power law (Schlichting, 1968) predict values that are consistantly different than those obtained by the Clauser method. A curve-fitted empirical relationship was developed from the present data and yields a better estimated value of C_f in the range $600 < Re_\theta < 2000$. It should be used only within this range for smooth-flat-plate flows in zero-pressure-gradient turbulent boundary layers.

REFERENCES

1. Bagnold, R. A., Physics of Blown Sand and Desert Dunes, Metheun and Company, Ltd., London, 1941.

2. Beavers, G. S., Sparrow, E. M, and Lloyd, J. R., "Low Reynolds Number Turbulent Flow in Large Aspect Ratio Rectangular Ducts," Journal of Basic Engineering, Vol. 93, 1971 pp. 296-299.

3. Clauser, F. H., "Turbulent Boundary Layers in Adverse Pressure Gradients," Journal of Aeronautical Sciences, Vol. 21, 1954, pp. 91-108.

4. Coles, D. E., "The Turbulent Boundary Layer in a Compressible Fluid," Rand Report 403-PR, 1962.

5. Coles, D. E., and Hirst, E. A., Proceedings of Computational Turbulent Boundary-Layers, Vol, II, Department of Mechanical Engineering, Stanford University, Stanford, California, 1968.

6. Greeley, R., White, B. R., Pollack, J. B., Iversen J. D., and Leach, R. N., "Dust Storms on Mars: Considerations and Simulations," NASA Technical Memorandum 78423, December, 1977.

7. Hess, S. L., Henry, R. M., Leovy, C. B., Ryan, J. A., Tillman, J. E., Chamberlain, T. E., Cole, H. L., Dutton, R. G., Green, G. C., Simon, W. E., and Mitchell, J. L., "Mars Climatology from Viking I after 20 Sols," Science, Vol. 194, 1976, pp 78-81.

8. Hornbeck, R. W., Numerical Methods, Quantum Publishers Inc., New York, 1975.

9. Huffman, G. D., and Bradshaw, P., "A Note on von Kármán's Constant in Low Reynolds Number Turbulent Flows," Journal of Fluid Mechanics, Vol. 53, 1972, pp. 45-60.

10. Kline, S. J., Reynold, W. C., Schraub, F. A., and Runstadler, P. W., "The Structure of Turbulent Boundary Layers," Journal of Fluid Mechanics, Vol. 30, 1967, pp. 741-773.

11. Krylov, V. I., Approximate Calculation of Integrals, The Macmillan Company, New York, 1962.

12. Kudva, A. K., and Sensonske, A., "Structure of Turbulent Velocity and Temperature Fields in Ethylene Glycol Pipe Flow at Low Reynolds Number," Journal of Heat and Mass Transfer, Vol. 15, 1972, pp. 127-145.

13. Ludwieg, H., and Tillmann, W., "Untersuchungen über die Wandschubspannung in Turbvulenten Reibungsschichten," Ing-Arch., Vol. 17, 1949, pp. 288-299; translated as "Investigations of the Wall Shearing Stress in Turbulent Boundary Layers," Nat. Adv. Comm. Aero., Washington,

14. MacMillian, F., "Viscous Effects on Flattened Pitot Tubes at Low Speeds," Journal of the Royal Aeronautical Society, Vol. 58, 1954, pp. 837-839. Owen, T. and Biemann, K., "Composition of the Atmosphere at the Surface of Mars: Detection of Argon-36 and Preliminary Analysis," Science, Vol. 193, 1976, pp. 801-803.

15. Patel, V. C., "Calibration of the Preston Tube and Limitations on its Use in Pressure Gradients," Journal of Fluid Mechanics, Vol. 23, 1965, pp. 185-208.

16. Patel, V. C., and Head, M. R., "Some Observations on Skin Friction and Velocity Profiles in Fully Developed Pipe Channel Flows," Journal of Fluid Mechanics, Vol. 38, 1969, pp. 181-201.

17. Schlichting, H., Boundary Layer Theory, 6th Edition, Mcgraw-Hill Book Company, Inc., New York, 1968.

18. Simpson, R. L., "Characteristics of Turbulent Boundary Layers at Low Reynolds Numbers With and Without Transpiration," Journal of Fluid Mechanics, Vol. 42, 1970, pp. 769-802.

19. Vennard, J. K., and Street, R. L., Elementary Fluid Mechanics, 5th Edition, John Wiley & Sons, Inc., 1975.

20. White, F. M., Viscous Fluid Flow, McGraw-Hill Book Company, Inc., New York, 1974.

APPENDIX A

Empirical Expressions for the Skin-Friction Coefficient

Presented here are a few of the generally accepted empirical relations that were used to determine the skin-friction coefficient for low-Reynolds-number turbulent-boundary-layer flows on a smooth flat plate with zero pressure gradient.

(i) 1/7th-power-law relation (Schlichting, 1968)

This expression,

$$C_f = 0.0256\ Re_\Theta^{-1/4}\ , \qquad \text{(A-1)}$$

is derived from the 1/7th-power law of velocity distribution on a smooth flat plate, which follows from a similar development in pipe flow. This formula is limited to $U_\infty\ \delta/\nu < 100{,}000$; or, assuming $\Theta/\delta \cong 0.1$, $Re_\Theta < 10{,}000$. The form of the equation implies a lower limit corresponding to a value of Re_Θ where the boundary layer is fully developed. From the present study, this appears to be $Re_\Theta = 425$.

(ii) Ludwieg and Tillmann (1950)

The expression is

$$C_f = 0.246\ Re_\Theta^{-0.268}\ 10^{-0.678H}\ . \qquad \text{(A-2)}$$

The authors claim this to be accurate to within 3% over the range $1000 < Re_\theta < 40{,}000$.

(iii) White (1974)

This curve-fitted expression, based on Coles' constants for the "law of the wall" of $\kappa = 0.41$ and $B = 5.0$, is believed to be developed from the data compiled at the Stanford conference. It has the form

$$C_f = (0.3\, e^{-1.33H})/(\log Re_\theta)^{1.74-0.31H} \quad . \qquad \text{(A-3)}$$

A reasonable lower limit to the validity of this approximation is $Re_\theta = 1000$.

APPENDIX B

Experimental Facility

The experiments were performed in an environmental wind tunnel located at NASA's Ames Research Center in Moffett Field, California. The wind tunnel is housed in a concrete chamber which is capable of evacuation to Martian atmospheric pressures. The chamber is contained inside a large tower building. This tower, shown in Figure B-1, was originally built for acoustic and dynamic testing of rockets at low pressures. It has a height of 30 meters and a total volume of 4000 cubic meters, and is suitable for a variety of low-pressure experiments. The vacuum is supplied by a five-stage stream ejector plant, also located at NASA, which is capable of evacuating the chamber to pressures of less than 1% of atmospheric in around 40 minutes. The test area may be observed from the control room through a Plexiglas window which is 5 cm thick.

The wind tunnel, a schematic of which is shown in Figure B-2, consists of five seperable sections, each 2.4 meters in length, plus a 1-meter entrance section. This tunnel has an overall length of 13 meters. The first section contains the entry cone and flow straightners, the next is a boundary layer development section, the third section, which is enclosed in Plexiglas, contains the test area, and the last two sections are diffusers. A zero-pressure-gradient flow is created by an increasing cross-sectional area with increasing downsteam distance. This flow is produced by high-pressure air which is ejected through a network of 72 equally spaced orifices located at the end of the fourth section. This system is capable of producing a flow

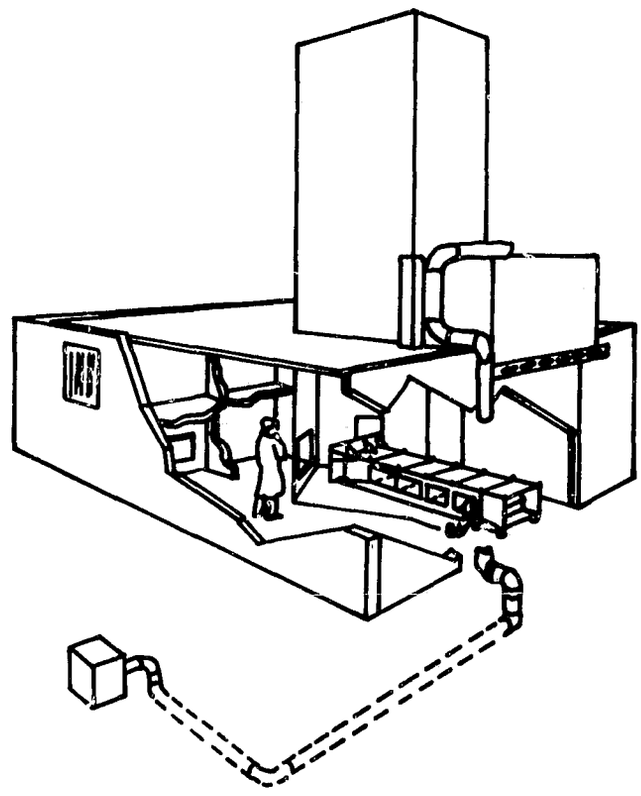

Figure B-1

Schematic diagram of the open-circuit wind tunnel showing the low-pressure chamber and control room.

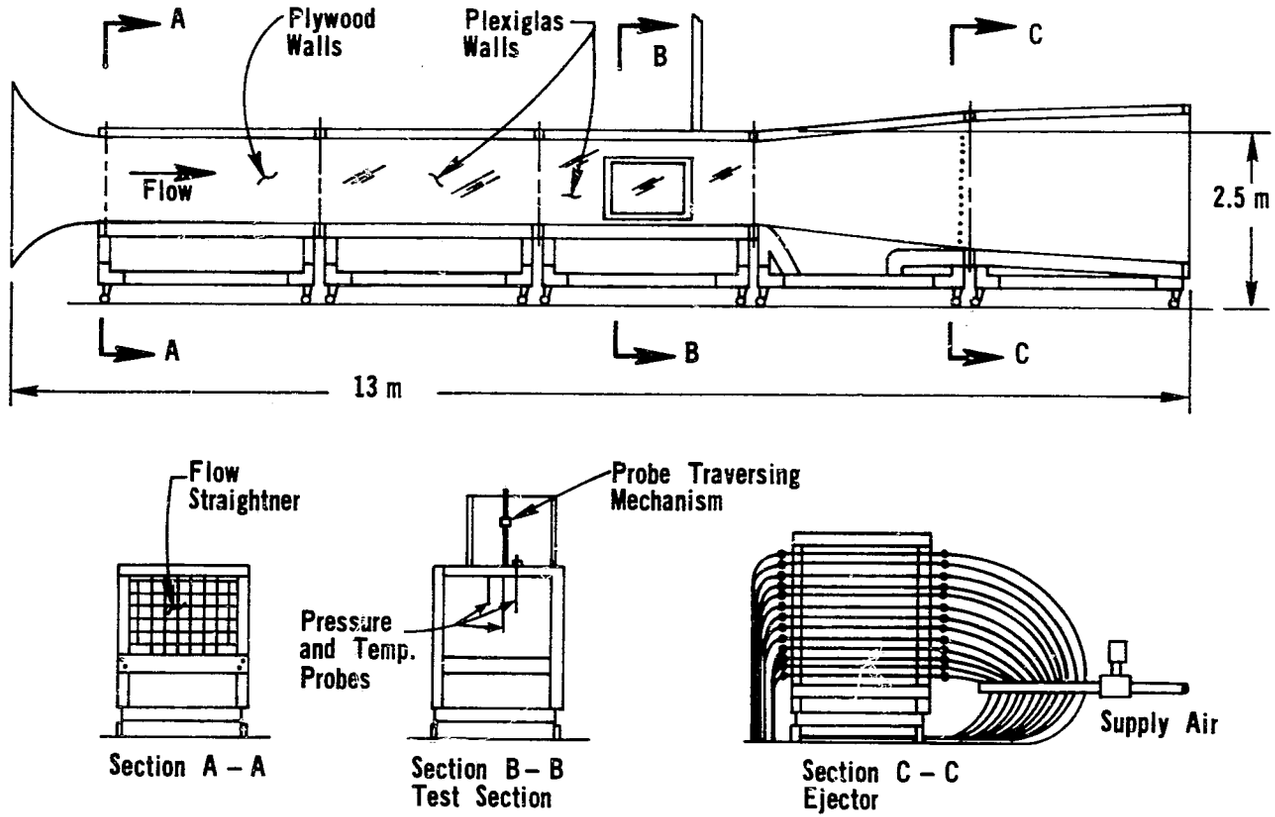

Figure B-2

Diagram of the wind tunnel showing entrance cone and flow straighteners (Section A-A), test section with various probes (Section B-B), and diffuser drive system (Section C-C).

speed of 12 m/s at atmospheric pressure and 170 m/s at 1/2% of atmospheric pressure. Although at atmospheric pressures a naturally turbulent boundary layer occurs inside the tunnel, at the lowest pressures it is necessary to trip the flow in order to induce a uniform transition to a turbulent layer. This tripping is produced by a bed of small pebbles that are attached to the tunnel floor in the first section. Since the pebbles are located more than 25 boundary layer thicknesses upstream of the test section, a fully developed turbulent core region exists at low pressures.

Experiments performed within the tower are controlled and the data recorded from the control room. Separate control panels are used to control the tower and the wind-tunnel operations. The wind tunnel is equipped with two sets of Pitot tubes, both with the tradename "Barocels". One of these measures free-stream pressure differentials from which speeds are calculated and is fixed in the tunnel. It is a type 571, 0-10 torr differential. The other is used to calculate boundary layer profiles from pressure differentials and is attached to a tranverse mechanism. This transducer is a type 538, 0-10 torr differential. Measurements are recorded on a two-channel strip chart recorder. The ambient pressure within the tunnel is measured with a "Barocels" type 570, 0-100 torr absolute. The tower ambient pressure is measured by three separate gauges which accurately cover the pressure range which the tower can maintain. One is a Wallace & Tiernan (Model FA 160) with a range of 0.1 to 20 torr. The second is also a Wallace & Tiernan gauge, Model FA 129. This gauge reads from 0 to 800 torr and is accurate to 5 torr. The third device is an electronic barometer. The signal is taken from a sensor mounted inside the tower. The stagnation temperature is measured from a thermocouple probe located within the tunnel. The probe is a United Sensor, silver-plated,

total temperature, Chromel-Alumel thermocouple. It is mounted in the ceiling of the tunnel upstream of the Pitot probes.

The tunnel was originally run with air as the working fluid. Modifications to the chamber have enabled the simulation of the Martian atmosphere by filling the chamber volume with carbon dioxide (CO_2). This is achieved by evacuating the tower to 0.39% atmospheric pressure, then filling with CO_2 to 7.9% atmospheric, resulting in a 95% CO_2 - 5% air mixture which closely resembles the Martian atmosphere. This mixture then may be pumped down to lower pressures by the steam ejector plant which further increases the similarities to Mars.

The data used in this research cover a wide range of pressures, from 0.3% to 100% atmospheric, and free-stream velocities from 4 to 96 m/s for working fluids of both air and carbon dioxide. This represents a range of momentum-deficit thickness Reynolds numbers Re_θ from less than 300 to over 7000, or in terms of the Reynolds number based on downstream distance Re_x: $90{,}000 < Re_x < 2{,}210{,}000$.

APPENDIX C

Computation of the Velocity Profile

In the following analysis, the flow is assumed to be isentropic. This assumes no heat transfer to or from the fluid, and a frictionless flow. For the boundary layer profiles under consideration, there is little opportunity for heat transfer to occur. Temperature gradients between the free-stream fluid and the plate are small, and the flow is moving at a speed greater than 5 m/s. The viscous effects are confined to the wall region, and are small for gases.

For a compressible ideal fluid, the isentropic flow characteristics may be expressed in terms of the stagnation conditions and local Mach number. As derived in Vennard & Street (1975) the local velocity may be expressed as

$$u^2 = c_p T_0 [1-(P/P_0)^{(\gamma-1)/\gamma}], \qquad (C\text{-}1)$$

where c_p is the specific heat,

T_0 the stagnation temperature

P_0 the stagnation pressure,

P the static pressure, and

γ the ratio of specific heats (c_p/c_v)

The theoretical velocity profile is then obtained by using the stagnation temperature measured in the wind tunnel, using the chamber pressure H_0 as the stagnation pressure, and ignoring viscous effects (isentropic assumption)

approximating the static pressure as $H_0-\Delta P$, where ΔP is the pressure differential from the boundary layer profile measured with Pitot and static tubes.

In order to calculate the temperature-dependant fluid properties, the temperature distribution within the velocity profile is calculated. Assuming perfect gas behavior and isentropic flow (i.e., M<1) the temperature distribution is found from the velocity profile by using the expression

$$T = T_0 - u^2/2c_p \ . \qquad (C\text{-}2)$$

Using this temperature profile, the absolute viscosity is calculated. The equations used for the gas properties, of course, depends on whether the fluid is air or CO_2. These and other expressions (or constants) are listed in Table C-1.

TABLE C-1

NUMERICAL VALUES OF FLUID PROPERTIES *

PROPERTY	AIR	CO_2
Specific heat (m^2/s^2K)	$c_p = 1005$	$c_p = 469. + 1.34\ T$ †
Specific heat ratio	$\gamma = 1.4$	$\gamma = 1.44 - 5.22 \times 10^{-4}\ T$ †
Gas constant (m^2/s^2 K)	$R = 287.$	$R = 189.$
Dynamic viscosity (g/cm s)	$\mu = \frac{2.62\ T^{3/2}}{1.80\ T + 199.}$	$\mu = \exp(0.00312\ T - 9.75)$

* All temperatures T are measured in Kelvins

† Valid only in the temperature range $253 < T < 303$ K

The local Mach number is calculated from

$$M = u/\sqrt{\gamma RT} \ . \qquad (C\text{-}3)$$

Using this value, the density is found from the relation

$$\rho = (H_0/RT_0)\ \{1+[M^2(\gamma - 1)/2]\}^{\gamma/(1-\gamma)} \ . \qquad (C\text{-}4)$$

The kinematic viscosity is easily found from

$$\nu = \mu/\rho \ . \qquad \text{(C-5)}$$

In order to correct for viscous effects on the Pitot probe, the local Reynolds number based on the probe diameter D is calculated as

$$Re_D = D\ u/\nu \ , \qquad \text{(C-6)}$$

where D = 0.0425 cm. The corrected local velocity is then found from the theoretical velocity using a pressure coefficient C which is determined from Re_D. The corrected velocity is

$$u_{corrected} = u_{theoretical} \sqrt{C} \ , \qquad \text{(C-7)}$$

where the pressure coefficient is found for the appropriate region (as suggested by MacMillian, 1954) from

$$\begin{aligned} C &= -0.0680\ \ln(Re_D) + 1.16, && 0. < Re_D < 13.6; \\ C &= 0.00372\ \ln(Re_D) + 0.974, && 13.6 < Re_D < 1000; \\ C &= 1, && Re_D > 1000. \end{aligned} \qquad \text{(C-8)}$$

APPENDIX D

Integration of the Square of the Velocity Profile

A general family of numerical integration formulas is the Newton-Cotes quadrature formulas described by Krylov (1962). These formulas are more accurate than the trapizoidal rule and Simpson's rule for integration over a finite interval (Hornbeck, 1975).

As shown in Eq. (3), the momentum-deficit thickness can be found from

$$\Theta/\delta = \int_0^1 u/U_\infty \; d(y/\delta) - \int_0^1 (u/U_\infty)^2 \; d(y/\delta) \quad . \qquad \text{(D-1)}$$

The first integral is easily found from the cubic spline curve fit to the velocity profile data. The second integral is not as directly evaluated, involving the square of the profile.

Assuming that the velocity profile is represented by a 4th order cubic spline, the profile is broken up into 4 sections, as shown in Figure D-1. This cubic spline fit is determined from the velocity profile reduction routine. The endpoints of the cubics are stored in a vector XK which has 5 values in it, ranging from XK_1= 0 to XK_5=1. The coefficients of the cubic spline are located in the vector YO (of length 4) and the matrix C (of order 4 by 3). In order to determine the velocity S at a height T, the first step is to determine which section of the profile the height T corresponds to, that is, to determine I so that XK(I) $\leq$ T $<$ XK(I+1). Using the coefficients of the cubic for this section the velocity is found from

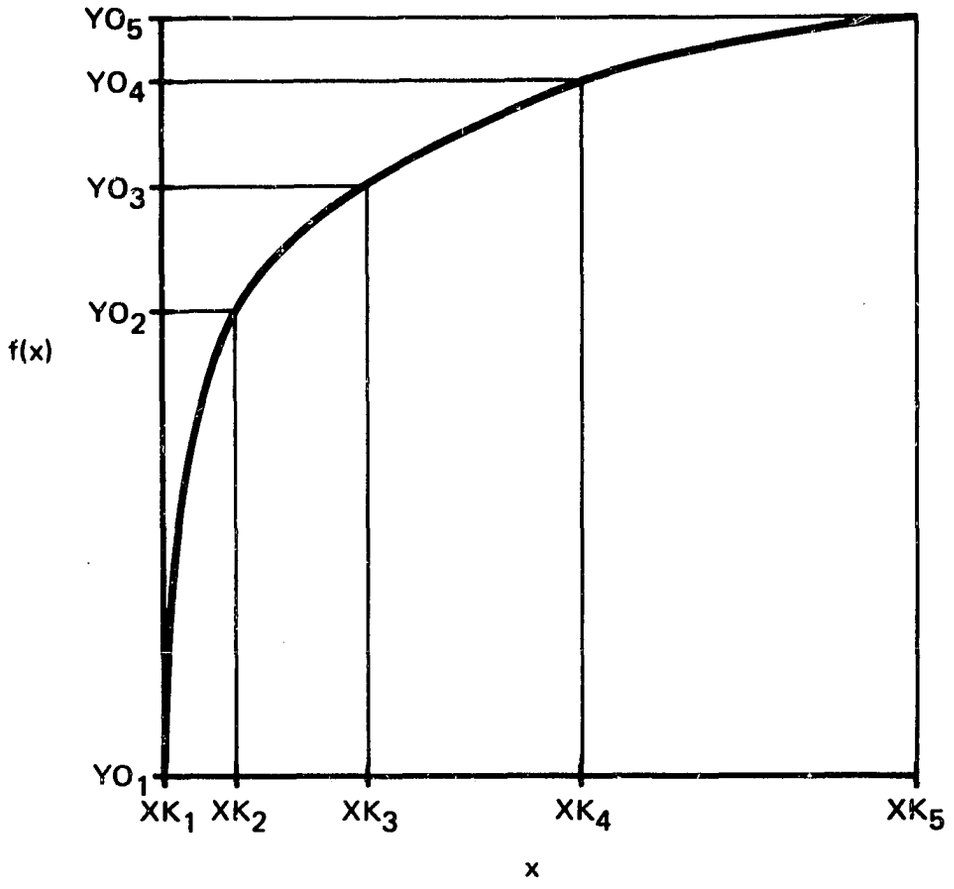

Figure D-1

Sections for the cubic spline curve fit of a boundary layer profile (not to scale).

$$S(T) = C(I,3)\ D^3 + C(I,2)\ D^2 + C(I,1)\ D + YO(I) \quad , \qquad \text{(D-2)}$$

where $D = T-XK(I)$.

From this curve fit, the velocity predicted by the cubic spline can be found for any height within the boundary layer profile.

Using the cubic spline representation of the velocity profile, the integral over the interval from 0 to 1 is equivalent to the sum of the integrals over each section of the spline. Thus, for the normalized velocity profile this becomes

$$\int_0^1 (u/U_\infty)^2 \ d\ (y/\delta) = \sum_{I=1}^{4} \int_{XK(I)}^{XK(I+1)} (u/U_\infty)^2\ d(y/\delta) \quad , \qquad \text{(D-3)}$$

where the cubic equation is substituted for the velocity in the corresponding section.

Using a seventh-order Newton-Cotes formula for integration, each section is divided into 7 equal segments of length

$$h = [XK(I+1)-XK(I)]/7 \ . \qquad \text{(D-4)}$$

The seventh order Newton-Cotes formula may be written as

$$\int_{XK(I)}^{XK(I+1)} f(x)\ dx = [XK(I+1)-XK(I)] \sum_{k=1}^{B} B_k\ f(XK(I)+k\cdot h) \quad , \qquad \text{(D-5)}$$

where the coefficients B_k are tabulated in Table D-1 and $f(XK(I)+k\cdot h)$ is found from squaring the velocity predicted by the cubic spline at the height $XK(I)+k\cdot h$.

TABLE D-1

VALUES OF THE COEFFICIENTS USED IN THE SEVENTH-ORDER NEWTON-COTES FORMULA

$B_1 = 751 / 17280$
$B_2 = 3577 / 17280$
$B_3 = 1323 / 17280$
$B_4 = 2989 / 17280$
$B_5 = B_4$
$B_6 = B_3$
$B_7 = B_2$
$B_8 = B_1$

APPENDIX E

Slip Velocity Effects

The treatment of fluids as a continuum is based on the assumption that the mean free path λ of the molecules is insignificant compared with the dimensions of interest. In this case, the properties of the gas depend primarily upon the frequency and character of the intermolecular collisions. As the pressure is lowered, the frequency of these collisions is also reduced. At the low densities, the collisions of the molecules with the constraining walls becomes as important as the intermolecular collisions. Though still small, the mean free path is no longer negligible compared to the body dimensions. Each molecule acts independently of the others.

In viscous flows at low densities the gas begins to slip over the surface of the boundaries. On a molecular scale even the smoothest surfaces appear rough. Gas molecules which strike the walls are reflected at some random angle uncorrelated with their entry angle. This is termed diffuse reflection and is very similar to the scattering of light rays as they reflect off dull surfaces. Applying the conservation-of-momentum principle to the reflecting surface requires that the lack of reflected tangential momentum be balanced by a finite slip velocity u_w of the wall relative to the adjacent fluid.

The reflection of gases off surfaces may be treated as perfectly diffuse reflection. The resulting slip velocity is related to the mean free path by the expression

$$u_w = \lambda \left.\frac{du}{dy}\right|_w . \qquad \text{(E-1)}$$

After simple substitutions, White (1974) arrived at the relation

$$u_w/U_\infty = 0.75\ M\ C_f , \qquad \text{(E-2)}$$

where M is the Mach number of the free stream. This expression can be used to measure the importance of slip flow for a given flow situation.

The effects of slip flow are greatest in flows with low densities and high wall shearing stresses. Using values from the experimental profiles listed in Table 1, it was found that slip flow is of no concern in these profiles. Table E-1 lists the importance of slip velocities for some profiles. These profiles were deemed to have the highest amount of slip because of the low pressures coupled with high skin-friction coefficients. It can be seen that the ratio of slip velocity to free-stream speed reaches a maximum of 0.13%. This effect is too small to be measured with the existing apparatus.

TABLE E-1

EFFECTS OF SLIP FLOW FOR LOW PRESSURE FLOWS

Pressure (% atm)	Mach Number	C_f x 1000	u_w/U_∞* (%)
0.39	0.369	4.81	0.13
0.38	0.348	4.75	0.12
0.39	0.371	4.50	0.13
0.39	0.324	4.81	0.12
0.43	0.328	4.43	0.11
0.46	0.335	4.40	0.11
0.68	0.123	4.80	0.044

*Eq. (E-2)